A TRANSVERSELY ISOTROPIC VISCOELASTIC BIPHASIC MODEL OF ARTICULAR CARTILAGE IN UNCONFINED COMPRESSION

By

ROMIT MAULIK

Bachelor of Engineering

Birla Institute of Technology

Ranchi, India

2012

Submitted to the Faculty of the
Graduate College of the
Oklahoma State University
in partial fulfillment of
the requirements for
the Degree of
MASTER OF SCIENCE
July, 2015

A TRANSVERSELY ISOTROPIC VISCOELASTIC BIPHASIC MODEL OF ARTICULAR CARTILAGE IN UNCONFINED COMPRESSION

Thesis Approved:

Dr. Hamed Hatami-Marbini

Thesis Adviser

Dr. Sandip Harimkar

Dr. Russell R. Rhinehart

ACKNOWLEDGEMENTS

This work was carried out under the watchful guidance of my adviser Dr. Hamed Hatami-Marbini. His patience and readiness to help me have been invaluable for all I have achieved. I would like to thank Dr. Rhinehart for his inputs on our optimization problems and also thank Dr. Harimkar for being a part of my defense committee.

I would also like to express my gratitude at the support and encouragement from my family and loved ones without which none of this would have been possible.

Romit Maulik
Stillwater, OK

Name: ROMIT MAULIK

Date of Degree: JULY, 2015

Title: A TRANSVERSELY ISOTROPIC VISCOELASTIC BIPHASIC MODEL OF ARTICULAR CARTILAGE IN UNCONFINED COMPRESSION

Major Field: MECHANICAL & AEROSPACE ENGINEERING

Articular cartilage is a connective tissue found in diarthrodial joints such as the knee, elbow or wrist. It is composed of collagen fibers, chondrocytes, interstitial fluid, and other non-collagenous proteins. During locomotion, the articular cartilage of the knee is primarily subjected to compressive stress caused by the upper body weight of the host. It is of great interest to investigate the mechanical behavior of this specialized connective tissue in compression and understand its ability to withstand high stresses without any damage. In recent years, unconfined compression experiments and biphasic numerical models have been widely used for this purpose.

The primary goal of this thesis was to develop an improved biphasic constitutive model for the mechanical behavior of cartilage in unconfined compression. For this purpose, the tissue was assumed to be composed of a transversely isotropic viscoelastic solid phase and an incompressible fluid phase. Using this premise, along with the classical biphasic material model assumptions, it was shown that the governing equilibrium equations can be simplified to two partial differential equations for the radial displacement of the solid phase and the pressure of the fluid phase. These coupled differential equations were solved and a numerical solution for the axial load intensity was obtained. The results of this computational model were then used to analyze previous experimental studies on articular cartilage. To this end, an optimization algorithm was used to conduct a non-linear least squares regression analysis and find the material parameters of the proposed model. It was observed that the proposed model could successfully predict the mechanical response of the tissue in high strain rate compression experiments with much greater accuracy as compared to most of the currently existing models in literature. For low strain rate compression experiments, although the model was able to represent the stress-relaxation behavior fairly accurately, higher residuals were obtained. This suggests that the solid phase viscoelasticity may play an important role in the overall stress relaxation mechanism of the tissue at high compressive strain rates. In conclusion, this research study provided a new analytic tool to investigate the mechanical stresses generated in an articular cartilage sample during unconfined compression.

TABLE OF CONTENTS

Chapter Page

1. Introduction **1**

1.1. Motivation 1

1.2. Experimental and Computational Investigations 2

1.3. Specific Aims of this thesis 3

1.4. Expected Outcomes 4

2. Background **5**

2.1. Structure & Composition of Articular Cartilage 5

2.2. Experimentation on Articular Cartilage 8

2.3. Compression experiments and Articular Cartilage - A Review of various formulations 13

2.4. Optimization 19

3. Transversely Isotropic, Viscoelastic and Biphasic Model **27**

3.1. Mathematics Prerequisites 27

3.2. The Biphasic Material Assumption 29

3.3. Solid Phase Constitutive Relationship 32

3.4. Incorporating Linear Viscoelasticity to Solid Phase 35

3.5. Solution of New Partial Differential Equations 37

3.6. Selective Viscoelasticity in Radial and Axial Directions 39

3.7. Investigation of Proposed Model 40

3.8. Curve Fitting 49

4. Conclusions and Future Work **54**

4.1. Conclusions 54

4.2. Future Work 55

4.2.1 Extension of Assumptions for Higher Complexity 55

4.2.2 Preliminary studies on Finite Difference Modeling 57

4.2.3 Preliminary Studies on Quasilinear Viscoelastic Modeling for Unconfined Compression 58

References **61**

Appendix A **71**

LIST OF FIGURES

Figures		Page
1	A schematic of the cross section of healthy articular cartilage. A shows chondrocyte organization & B shows Collagen Fiber Orientation (with permission from [1])	6
2	Rope like collagen fibrils and interspersed chondrocytes in articular cartilage (with permission from [2])	8
3	Articular Cartilage location in the Human Body. As shown here, the tissue prevents contact between the femur and the tibia which are the largest bones in the thigh and the ankle respectively (adapted from http://www.niams.nih.gov/)	9
4	Loading curves and indenter geometry for a general indentation experiment (with permission from [3]). The figure plots loading force with depth of penetration into material.	9
5	Specimen geometry for shear loading. θ is the angle of rotation generated by the torque transducer	10
6	Experimental geometry schematic for the uniaxial confined compression test with an NaCl bathing solution(with permission from [4])	11
7	Schematic for Unconfined Compression Test (with permission from [5]) .	12
8	A comparison of the isotropic and tranversely isotropic Models for infinitesimal deformation for the uniaxial unconfined compression of articular cartilage (with permission from [6])	14
9	Fig. (a) A ramp strain (b) A stress relaxation curve	17

10 Convergence Studies using three optimizers - Leapfrogging - Differential Evolution - Particle Swarm 24
11 Pseudocode for Leapfrogging optimizer. The OF value is the error between model and experimental data. A better OF implies lower error 25
12 Process flow for general evolutionary algorithm 26
13 Unconfined Compression Sample Geometry 33
14 Effect of Ramptime - Viscoelasticity in all directions. Model Parameters : E_1 = 4.55 MPa, E_3 = 0.47 MPa, ν_{21} = 0.3, ν_{31} = 0, k = 5x10^{-15}, c = 0.16, τ_1 = 0.06s, τ_2 = 201s, radius = 6.35mm, 10% strain 41
15 Effect of Ramptime - Viscoelasticity in E_1 direction. Model Parameters : E_1 = 4.55 MPa, E_3 = 0.47 MPa, ν_{21} = 0.3, ν_{31} = 0, k = 5x10^{-15}, c = 0.16, τ_1 = 0.06s, τ_2 = 201s, radius = 6.35mm, 10% strain 41
16 Effect of c - Viscoelasticity in all directions. Model Parameters : E_1 = 4.55 MPa, E_3 = 0.47 MPa, ν_{21} = 0.3, ν_{31} = 0, k = 5x10^{-15}, ramp time = 131s, τ_1 = 0.06s, τ_2 = 201s, radius = 6.35mm, 10% strain 42
17 Effect of c - Viscoelasticity in E_1 direction. Model Parameters : E_1 = 4.55 MPa, E_3 = 0.47 MPa, ν_{21} = 0.3, ν_{31} = 0, k = 5x10^{-15}, ramp time = 131s, τ_1 = 0.06s, τ_2 = 201s, radius = 6.35mm, 10% strain 42
18 Effect of τ_1 - Viscoelasticity in all directions. Model Parameters : E_1 = 4.55 MPa, E_3 = 0.47 MPa, ν_{21} = 0.3, ν_{31} = 0, k = 5x10^{-15}, ramp time = 131s, c = 0.16, τ_2 = 201s, radius = 6.35mm, 10% strain 43
19 Effect of τ_1 - Viscoelasticity in E_1 direction. Model Parameters : E_1 = 4.55 MPa, E_3 = 0.47 MPa, ν_{21} = 0.3, ν_{31} = 0, k = 5x10^{-15}, ramp time = 131s, c = 0.16, τ_2 = 201s, radius = 6.35mm, 10% strain 43
20 Effect of τ_2 - Viscoelasticity in all directions. Model Parameters : E_1 = 4.55 MPa, E_3 = 0.47 MPa, ν_{21} = 0.3, ν_{31} = 0, k = 5x10^{-15}, ramp time = 131s, c = 0.16, τ_1 = 0.06s, radius = 6.35mm, 10% strain 44
21 Effect of τ_2 - Viscoelasticity in E_1 direction. Model Parameters : E_1 = 4.55 MPa, E_3 = 0.47 MPa, ν_{21} = 0.3, ν_{31} = 0, k = 5x10^{-15}, ramp time = 131s, c = 0.16, τ_1 = 0.06s, radius = 6.35mm, 10% strain 44

22 Effect of ν_{21} - Viscoelasticity in all directions. Model Parameters : E_1 = 4.55 MPa, E_3 = 0.47 MPa, ν_{31} = 0, k = 5x10^{-15}, ramp time = 131s, c = 0.16, τ_1 = 0.06s,τ_2 = 201s, radius = 6.35mm, 10% strain 45

23 Effect of ν_{21} - Viscoelasticity in E_1 direction. Model Parameters : E_1 = 4.55 MPa, E_3 = 0.47 MPa, ν_{31} = 0, k = 5x10^{-15}, ramp time = 131s, c = 0.16, τ_1 = 0.06s,τ_2 = 201s, radius = 6.35mm, 10% strain 46

24 Effect of ν_{31} - Viscoelasticity in all directions. Model Parameters : E_1 = 4.55 MPa, E_3 = 0.47 MPa, ν_{21} = 0.49, k = 5x10^{-15}, ramp time = 131s, c = 0.16, τ_1 = 0.06s, τ_2 = 201s, radius = 6.35mm, 10% strain 46

25 Effect of κ - Viscoelasticity in all directions. Model Parameters : E_1 = 4.55 MPa, E_3 = 0.47 MPa, ν_{21} = 0.49, ν_{31} = 0.0, ramp time = 131s, c = 0.16, τ_1 = 0.06s, τ_2 = 201s, radius = 6.35mm, 10% strain 47

26 Effect of κ - Viscoelasticity in E_1 direction. Model Parameters : E_1 = 4.55 MPa, E_3 = 0.47 MPa, ν_{21} = 0.49, ν_{31} = 0.0, ramp time = 131s, c = 0.16, τ_1 = 0.06s, τ_2 = 201s, radius = 6.35mm, 10% strain 47

27 Effect of E_1/E_3 - Viscoelasticity in all directions. Model Parameters : E_3 = 1 MPa, ν_{21} = 0.49, ν_{31} = 0.0, k = 5x10^{-15}, ramp time = 131s, c = 0.16, τ_1 = 0.06s, τ_2 = 201s, radius = 6.35mm, 10% strain 48

28 Effect of E_1/E_3 - Viscoelasticity in E_1 direction. Model Parameters : E_3 = 1 MPa, ν_{21} = 0.49, ν_{31} = 0.0, k = 5x10^{-15}, ramp time = 131s, c = 0.16, τ_1 = 0.06s, τ_2 = 201s, radius = 6.35mm, 10% strain 48

29 Effect of radius - Viscoelasticity in all directions. Model Parameters : E_1 = 4.55 MPa, E_3 = 0.47 MPa, ν_{21} = 0.49, ν_{31} = 0.0, k = 5x10^{-15}, ramp time = 131s, c = 0.16, τ_1 = 0.06s, τ_2 = 201s, 10% strain 49

30 Effect of radius - Viscoelasticity in E_1 direction. Model Parameters : E_1 = 4.55 MPa, E_3 = 0.47 MPa, ν_{21} = 0.49, ν_{31} = 0.0, k = 5x10^{-15}, ramp time = 131s, c = 0.16, τ_1 = 0.06s, τ_2 = 201s, 10% strain 49

31 Curve fit for slow compression (Cartilage) under the assumption that viscoelasticity exists in all directions. Fit parameters: E_1 = 0.64 MPa, E_3 = 0.408 MPa, k = 3.6x10^{-15} c = 6.16, τ_1 = 141.9, τ_2 = 337.27, 5% strain, R^2 = 0.991 50
32 Curve fit for slow compression (Cartilage) under the assumption that viscoelasticity exists in E1 Direction. Fit parameters: E_1 = 4.19 MPa, E_3 = 0.408 MPa, k = 1.1x10^{-15} c = 0.69, τ_1 = 52.62, τ_2 = 112.204, 5% strain, R^2 = 0.992 51
33 Curve fit for fast compression (in normal time) under the assumption that viscoelasticity exists in all directions - Inconclusive near peak. Fit parameters: E_1 = 7.9 MPa, E_3 = 1.34 MPa, k = 0.78x10^{-15} c = 0.13, τ_1 = 0.054, τ_2 = 329.28, 5% strain, R^2 = 0.991 51
34 Curve fit for fast compression (in normal time) under the assumption that viscoelasticity exists in E1 direction - Inconclusive near peak. Fit parameters: E_1 = 8.7 MPa, E_3 = 1.34 MPa, k = 0.74x10^{-15} c = 0.14, τ_1 = 0.052, τ_2 = 236.03, 5% strain, R^2 = 0.991 52
35 Curve fit for fast compression (Cartilage) under the assumption that viscoelasticity exists in all directions. Fit parameters: E_1 = 7.9 MPa, E_3 = 1.34 MPa, k = 0.78x10^{-15} c = 0.13, τ_1 = 0.054, τ_2 = 329.28, 5% strain, R^2 = 0.991 52
36 Curve fit for fast compression (Cartilage) under the assumption that viscoelasticity exists in E1 direction. Fit parameters: E_1 = 8.7 MPa, E_3 = 1.34 MPa, k = 0.74x10^{-15} c = 0.14, τ_1 = 0.052, τ_2 = 236.03, 5% strain, R^2 = 0.991 53
37 A Comparison of FDM and Analytical Solutions 58
38 Curve fit for slow compression (Cartilage) using the new QLV model. Fit parameters: A = 1602.28 Pa, n = 0.402, c = 2.83, τ_2 = 152.18s, τ_1 = 1X10^{-3}, 10% strain, R^2 = 0.994 60

39 Curve fit for fast compression (Cartilage) using the new QLV model. Fit parameters: $A = 0.24$MPa, $n = 0.455$, $c = 1.97$, $\tau_2 = 820.89$s, $\tau_1 = 0.19$, 5% strain, $R^2 = 0.990$ 60

SYMBOLS AND ABBREVIATIONS

TI	Transversely Isotropic
BPVE	Biphasic - Poroviscoelastic
QLV	Quasi-Linear Viscoelasticity
TI BP	Transversely Isotropic Biphasic
PDE	Partial Differential Equation
$\bar{x}$	Laplace transformed x

CHAPTER 1

Introduction

1.1. Motivation

Soft tissue in the human body serves a variety of important functions according to their structure and location. Some important examples of soft tissue are the cornea (which is instrumental for proper vision), articular cartilage (which is fundamental for shock absorption and friction reduction), ligaments (which usually connect bone to bone) and tendons (which usually connect muscle to bone). Over the past few decades researchers have investigated the structure and mechanical response of these tissue in order to understand the underlying mechanisms of their functions. The primary purpose of their investigations is to be able to understand how disease and injury affect the structure and function of these tissue and to devise treatments (or to develop artificial implants) to improve the quality of life of their hosts.

In this thesis, the primary focus is to develop a constitutive model for the unconfined compression of articular cartilage. Cartilage is a flexible connective tissue present in areas like the joints between bones, the rib cage, the ear, the nose, the bronchial tubes and the inter-vertebral discs. They are avascular (i.e. they are devoid of blood supply) and are generally classified into three types elastic cartilage, hyaline cartilage and fibrocartilage, which differ in relative amounts of cartilage. Articular cartilage consists of both fibrocartilage and hyaline cartilage and is present in the joints of the knee. The mechanical properties of articular cartilage are of great importance in load bearing joints such as the knee and the hip and have thus been studied intensely at different scales of magnification [7, 8]. Cartilage of the knee has to deal with frictional, compres-

sive, shear and tensile loading and is thus very important to the quality of life of the host. However, articular cartilage is susceptible to diseases such as osteoarthritis which is a degenerative disease caused by the loss of tissue volume and is reported to affect upto 27 million people in the United States alone [9]. It is also somewhat unique in that it has relatively little ability to repair itself. One of the primary reasons for the investigation into the mechanics of articular cartilage is to devise synthetic substitutes for replacement of impaired tissue so as to prevent pain and loss of mobility.

1.2. Experimental and Computational Investigations

Researchers endeavor to develop explanations for the reasons soft tissue behave in their remarkable manner. Before coming up with theories to explain this behavior, it is vital to have examined the behavior of these tissue in a laboratory setting. To that end, scientists have devised experimental investigations which on implementation would allow a standard testing environment for different laboratories to compare results. A variety of configurations have been devised for these experiments so that different mechanical behavior of the tissue can be examined. In this body of work, the experimental configuration investigated was the unconfined compression experiment. Apart from this, scientists have undertaken confined compression, shear, indentation and tension experiments to determine the mechanical properties of the test samples.

Once a certain degree of familiarity is established about the behavior of tissue in experimental configurations, attempts are made to devise mathematical models to try to explain the mechanics of the samples. The modeling for these tissue has successively grown more accurate (and more complex) with greater understanding of the underlying phenomenon of their load bearing capacity. These theories are generated and adapted to the experimental configurations mentioned in the previous section and are used to try to determine the material properties of the tissue. Once formulated and validated, these theories also serve as a tool for different laboratories to characterize the mechanical properties for their specimen. Experimental data and theory are compared to each other using regression analyses which can be used to determine unique parameters for

each experiment thus allowing scientists to understand the features of this particular specimen in comparison to others.

Another important purpose for the developed theory is its use in finite element simulations which can be used to analyze significantly more complicated geometries such as in actual models for the cartilage in the knee. Several theories have been developed down the years for articular cartilage with varying levels of success. With greater insights of the structure of articular cartilage and improving computational speeds, greater degrees of complexity are being built into these theories.

There are several constitutive models (i.e. models which establish relationships between stress and an independent variable such as strain) in literature which have been used to predict the mechanical response of tissue in various experimental configurations. These models may be devised according to some underlying knowledge about the structure of the tissue or they may be purely empirical in nature. Empirical models are those that approach a particular problem from a mathematical point of view where the objective is to develop an expression that predicts a phenomenon rather than one that explains it. Many constitutive models are developed under the assumption that soft tissue can be approximated according to mixture theory (i.e. a theory which assumes that there are different phases that combine to form the macroscopic structure of the tissue). In addition, they also assume that the tissue has a time dependent response to mechanical loading (otherwise known as a viscoelastic response) and these assumptions are used to determine a material model for the behavior of the tissue in the laboratory environment. Experimental investigations have also revealed an anisotropic behavior of the specimen and this fact has also been taken into account in some research. A thorough review of literature provided us with the opportunity to devise our own material models using elements of the assumptions stated above in order to provide an improved estimate of the mechanical response of articular cartilage.

1.3. Specific Aims of this thesis

The specific aims of this thesis were -

1. Devising a constitutive model that assumes a dual phase (solid and fluid) tissue specimen with time dependent transverse isotropy in its solid phase for the unconfined compression experiment.

2. Thoroughly examining the behavior of the proposed model for the effect of its material parameters (a parametric study).

3. Curve fitting these models to some experimental data in order to determine the material parameters that describe a particular specimen. The curve fitting algorithms to be used were selected after a convergence study.

1.4. Expected Outcomes

At the conclusion of this thesis, it is expected that a greater understanding would be achieved of the mechanics that control the behavior of articular cartilage in the unconfined compression experiment. The new constitutive model developed would be a more accurate method to predict the stress response of specimen in unconfined compression. This model would then be examined using a parametric study which would enable us to understand the effect of each parameter on the hypothetical specimen. Unique material parameters would be obtained for the experimental data generated by a sample using optimization techniques. The performance of this newly developed model would be compared to an existing model in literature.

CHAPTER 2

Background

The purpose of this chapter is to introduce the reader to the various important phases in the work-flow and to give the reader a brief idea of the basic information behind each phase. These ideas will then form the foundation of the new work proposed in this thesis.

2.1. Structure & Composition of Articular Cartilage

Articular cartilage is a connective tissue commonly found in diarthroidal joints which are the most common type of movable joints such as those present in the joints of the knee and elbows as well as the carpals of the wrist. Its primary function is to provide a smooth, lubricated surface for the joint and for a low friction load bearing environment. This tissue is also characterized by being avascular (i.e. it is not supplied by blood vessels, lymphatics or nerves) and is subjected to a harsh biochemical environment [10].

Articular cartilage is classified as a hyaline cartilage and is generally 2-4 mm thick. Its principal constituents are water, collagen fibres and proteoglycans which combine with small amounts of other noncollagenous proteins and glycoproteins to form the ECM (or the extracellular matrix) with a sparse distribution of highly specialized cells called chondrocytes. These cells play a vital role in the development, maintenance and repair of the ECM and constitute about 2% of the volume of the articular cartilage [11].

In healthy articular cartilage, three distinct zones can be observed with each playing an important role in the overall function of the tissue. As shown in the schematic,

the thin superficial (or tangential) zone (STZ) protects the lower layers from shear stresses and may comprise approximately 10-20% of the cartilage thickness. This layer is characterized by tightly packed collagen fibers aligned parallel to the articular surface. The middle zone (as the name suggests, situated beneath the superficial zone) accounts for 40-60% of the total cartilage volume and is characterized by oblique collagen fibres. This zone accounts for a part of the compressive load bearing ability of the cartilage. The deep zone accounts for 30% of the cartilage volume approximately and accounts for a large part of the compressive load bearing ability of the cartilage due to the perpendicular arrangement of collagen fibres to the articular surface. This zone is also characterized by comparatively low water content as compared to the other two zones. There exists a calcified layer beneath the deep zone that secures the cartilage to the bone by anchoring the collagen fibrils of the overlying deep zone to the bone beneath it.

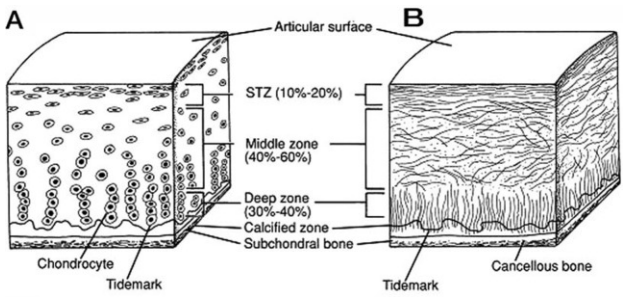

Figure 1: A schematic of the cross section of healthy articular cartilage. A shows chondrocyte organization & B shows Collagen Fiber Orientation (with permission from [1])

Another method of classification of articular cartilage is according to proximity to the resident cells of the cartilage (i.e. the chondrocytes). One of these regions is the pericellular matrix which is a thin layer adjacent to the chondrocyte cell membrane and it completely surrounds the chondrocyte. This region consists mainly of proteoglycans, glycoproteins and other noncollagenous proteins. It has been hypothesized that this region initiates signal transduction within cartilage on load bearing [12]. Immediately surrounding the pericellular matrix is the territorial matrix which is composed of fine collagen fibrils. This zone is credited with being a protective layer around the chon-

drocytes preventing it from injury due to mechanical stresses and contributing to the cartilage's ability to withstand large loads [13, 14]. The territorial matrix is surrounded by the inter-territorial region which is the largest of the three matrix regions. This matrix is characterized by bundles of collagen fibrils oriented in accordance with the zone they are situated it (i.e. perpendicular to the articular surface in the deep zone, oblique in the middle zone and parallel to the articular surface in the superficial zone).

In healthy articular cartilage, water accounts for upto 80% of the wet weight of the tissue. Around 30% of the water is contained in the intrafibrillar space within the collagen [15, 16]. Most of the rest is contained in the pore space of the matrix and a small amount is contained in the intracellular space. The relative water concentration is highest in the superficial zone and it continuously reduces with depth from the articular surface. A major importance of water in the tissue is that it helps to transport and distribute nutrients to the chondrocytes in addition to a being a lubricating mechanism. Much of the water in the ECM (i.e. in its pores) can be moved through it by applying a pressure gradient across the tissue or by applying a compressive load on it. The frictional resistance against this motion is very high leading to very low values of fluid permeability. This low permeability combined with the pressurization of water forms the basic mechanism by which the tissue derives its ability to withstand high loads [1].

Collagen is the most abundant macromolecule in the ECM and makes up for 60% of the dry weight of the cartilage. A major component of these are type II collagen which is fibrillar in nature. Other types of collagen are also found in the cartilage but they only constitute around 5% of the total collagen in the ECM. Proteoglycans are the second largest group of macromolecules in the ECM and account for around a tenth of the tissue's wet weight. They are important as they provide the cartilage with its osmotic properties which are critical to its ability to withstand compressive loads and are synthesized by the chondrocytes and secreted into the ECM.

Nutrition of the cartilage tissue occurs by diffusion from the synovial fluid (i.e. the fluid in the joint around the cartilage and bone). Due to a lack of blood supply or lymphatics, chondrocytes depend on anaerobic metabolism (i.e. metabolism in the absence of oxygen). Inactivity of the joint has been seen as a factor in impaired metabolism

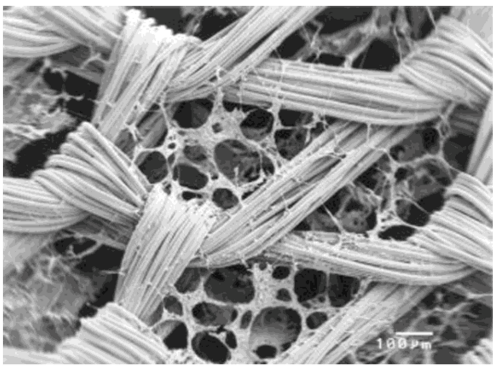

Figure 2: Rope like collagen fibrils and interspersed chondrocytes in articular cartilage (with permission from [2])

of the chondrocytes in the cartilage which causes its degradation. Therefore regular joint movement and dynamic loading is important for the maintenance of healthy articular cartilage. Diseases such as osteoarthritis is associated with large changes in the metabolism of chondrocytes and thus causes an imbalance in the degradation-turnover cycle of the ECM constituents synthesized by chondrocytes [17].

2.2. Experimentation on Articular Cartilage

As introduced in the previous chapter, scientists have devised several experimental procedures to analyze the behavior of articular cartilage under different types of mechanical loading. These experiments are primarily aimed at capturing creep or stress relaxation data caused by an applied load or a strain respectively. Loading done for experimentation may also be dynamic in nature which allows for recording the behavior of cartilage to alternative cycles of tension and compression. In this work we will be focusing primarily on compression testing, in particular the unconfined compression test geometry.

Some notable types of experimental tests include indentation tests [18, 19, 20, 21, 22]. These tests provide information about material properties from the indenter load and depth of indentation measured during loading and unloading of the material. They have been used to characterize mechanical properties by studying creep in metals [23] and

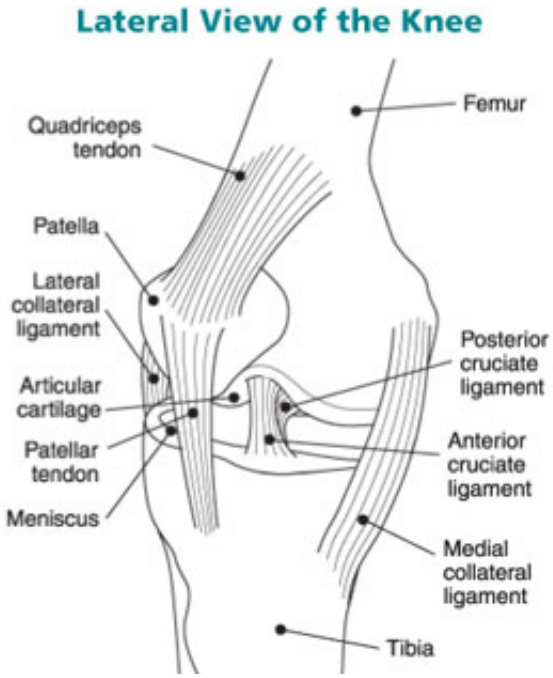

Figure 3: Articular Cartilage location in the Human Body. As shown here, the tissue prevents contact between the femur and the tibia which are the largest bones in the thigh and the ankle respectively (adapted from http://www.niams.nih.gov/)

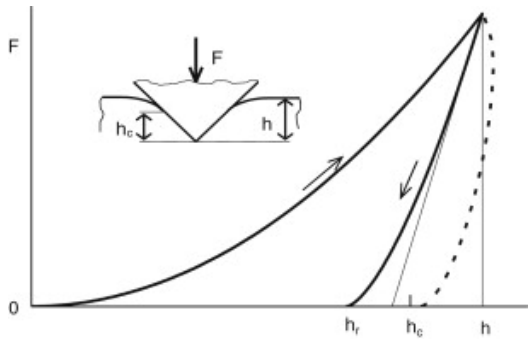

Figure 4: Loading curves and indenter geometry for a general indentation experiment (with permission from [3]). The figure plots loading force with depth of penetration into material.

glassy materials and by studying the viscoelastic behavior of polymers and other soft materials [24]. The indenter may be conical [25] (as shown in the figure 4) or circular

[26] and plane ended (such as a cylinder) or a rigid sphere.

The shear properties of articular cartilage are characterized by torsion testing devices which apply a deformation on the specimen as shown in the figure 5. This configuration allows for examination of the shearing behavior of the cartilage and allows for calculation of shear moduli [27, 28]. Alternatively, a dynamic application of shear strain may also be utilized here [29]. The application of load may be through fixing one end of the specimen and imparting a deformation through a torque transducer on the other end or it may be through a biaxial torsion tester with both ends being twisted to provide a deformation.

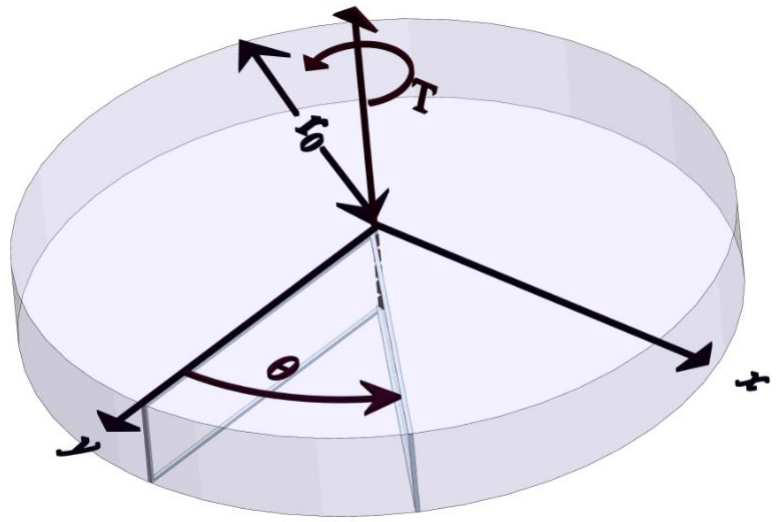

Figure 5: Specimen geometry for shear loading. θ is the angle of rotation generated by the torque transducer

Unaxial tensile tests are also quite popular for studying the mechanics of various soft tissue. They are commonly used for a variety of tissue such as cornea and ligaments which are subjected to tensile stresses in their natural environment [30, 31, 32]. In the uniaxial tensile test, the specimen is excised from the tissue in the form of a rectangular piece and clamped into position by securing both ends to prevent sliding. One end is commonly fixed and the other is used to impart a displacement or force load to the

sample.

The mechanical properties of articular cartilage are primarily investigated through the use of compression testing experiments such as unconfined or confined compression experiments. The articular cartilage of the knee is generally under great compressive loads (the upper body weight of the person) and their properties in compression are of great importance to the medical profession. In these types of experiments a cylindrical sample of cartilage is loaded with a compressive strain or force load in the axial direction. In a confined compression test, the cartilage specimen is sealed on the lateral sides to prevent any sort of radial displacement. The specimen is compressed between two plates in which the lower one is rigid and impermeable whereas the upper one is rigid and free draining [33, 34, 35].

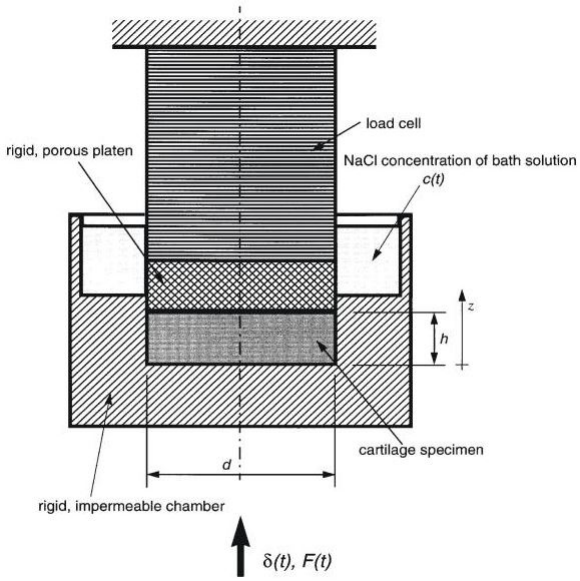

Figure 6: Experimental geometry schematic for the uniaxial confined compression test with an NaCl bathing solution(with permission from [4])

Modeling the mechanical behavior of cartilage in unconfined compression is the primary focus of our investigation in this thesis. The unconfined compression geometry consists of two rigid impermeable plates with a lower fixed one and an upper movable one. The load or strain displacement is applied by the movable platen. In contrast to

the confined compression experiment, the lateral sides of the cartilage specimen are not sealed and the specimen is free to be displaced in the radial direction. In this geometry, the specimen is surrounded by a bathing solution such as NaCl to prevent dehydration of tissue (the water content in the tissue causes a significant effect on the mechanical properties of the tissue). The lateral displacement of the solid also causes the development of a fluid pressure gradient in the radial direction [36].

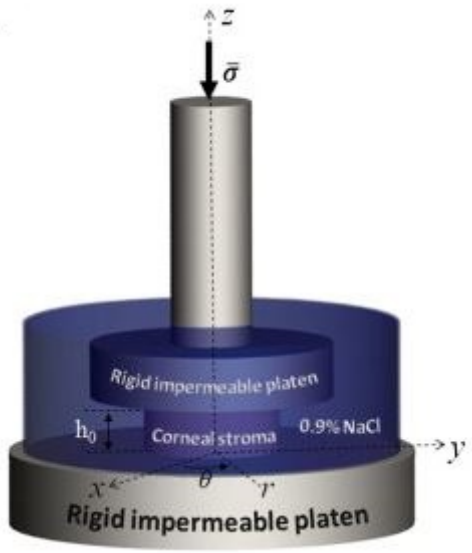

Figure 7: Schematic for Unconfined Compression Test (with permission from [5])

2.3. Compression experiments and Articular Cartilage - A Review of various theoretical formulations

As mentioned above, the compressive load bearing behavior of cartilage is of great interest to researchers due its vital function of supporting the compressive load due to the upper body weight in humans. Researchers have subjected articular cartilage to both confined and unconfined compression and have then tried to develop predictive mathematical models for the mechanical response of the cartilage specimen. One of the landmark works on the compressive behavior of articular cartilage was by Mow et al [35], where the articular cartilage tissue was modeled as a macroscopic structure with two phases in confined compression. This formulation assumed that the domain of the articular cartilage could be differentiated into a solid phase and a fluid phase. Two versions of the formulation were developed with one being an assumption for constant fluid permeability and the other prescribing a non-linear permeability for the specimen under varying dilatation.

Lai et al [37] extended the biphasic model to account for a strain rate dependent permeability. In their work, the fluid permeability was assumed to vary with strain rate applied during the loading of the tissue. The biphasic assumption coupled with constant fluid permeability has been a popular formulation due to its simplicity and was extended to the unconfined compression geometry by Armstrong [36]. Holmes in 1985, performed experiments to measure the strain rate dependent permeability and incorporated the results into a biphasic model for uniaxial compression experiments to obtain accurate stress and displacement fields in the cartilage specimen. Although the purely biphasic model was a breakthrough in the modeling of cartilage, it performed poorly in case of unconfined compression experiments. As a result of this, researchers have progressively added more complexity in order to search for a more accurate estimation of the stresses and displacements generated in the specimen. With more knowledge of the underlying physiology of the cartilage, better mathematical approximations were introduced to try and predict the mechanical behavior of specimen.

The biphasic assumption along with constant permeability was used by Mak [38] to

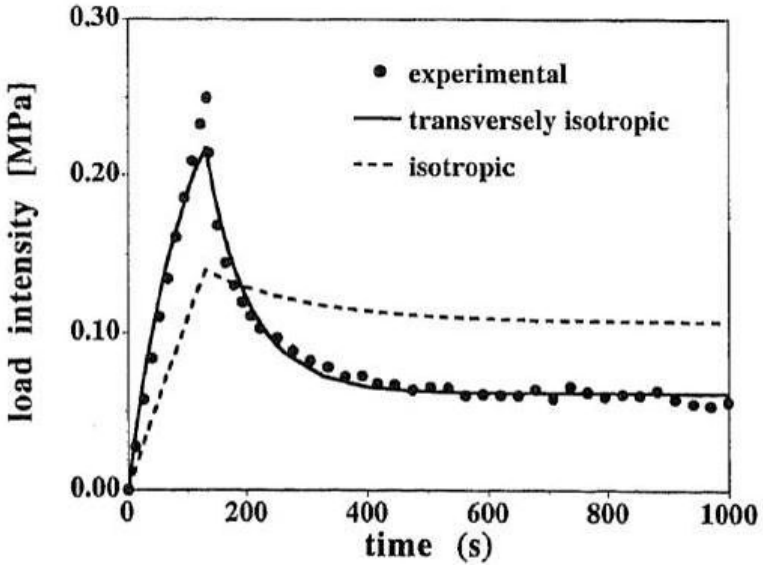

Figure 8: A comparison of the isotropic and tranversely isotropic Models for infinitesimal deformation for the uniaxial unconfined compression of articular cartilage (with permission from [6])

model a specimen with a linearly viscoelastic solid phase thus adding another mechanism of stress relaxation or creep to the problem. Prior to this it was assumed that the stress relaxation and creep behavior of cartilage was predominantly due to the friction between the fluid and solid phase caused by the extremely low permeability of the fluid in the ECM. Mak assumed that the solid phase also contributed to the stress relaxation behavior and formulated his problem for both the confined and unconfined compression apparatus. To adapt these formulations to large strain experiments, finite deformation formulations were also developed (so far most models assumed a small deformation experiment only). Researchers used the two-phase assumption and coupled it with finite deformation length scales to obtain continuum models which could either have strain dependent permeability or constant permeability throughout the specimen [39]. The assumption of solid phase viscoelasticity has also been combined with finite deformation models [40].

Higher complexity was added to the mathematical formulations in order to obtain a more accurate prediction of the displacement and pressure fields generated in the speci-

men during loading. Lai developed a three phase model for the deformation of cartilage in confined compression [41]. The assumptions behind the addition of the third phase were based on the fact that a third ion phase would exert an physico-chemical influence on the total stress of the mixture due to the charge-to-charge repulsive forces within the solid matrix. Cohen [6] ignored the electrochemical nature of the cartilage mixture and proceeded with an assumption that the solid phase of the cartilage was anisotropic in nature. In particular, it was assumed here that the cartilage was transversely isotropic with the plane of isotropy being in the radial direction. This modification (combined with the usual biphasic and constant permeability assumption) led to a physiologically accurate estimation of the stresses generated in the unconfined compression experiment (as anisotropic responses for articular have generally been described in experimental investigations). As we can see, additional layers of complexity have been added to the initial assumption of a simple two-phase mixture used to model the cartilage sample. Soltz used Curnier's conewise linear elasticity [42] in the place of linear elasticity in a biphasic model for the compression of cartilage [43]. This was also modified to include linear viscoelasticity by Huang [44]. Conewise linear elasticity is characterized by different responses to tension and compression loading which could be a feature of the behavior of cartilage.

However, there exists a gap in the literature here as the transversely isotropic model for the unconfined compression experiment was not extended to account for solid phase viscoelasticity for infinitesimal deformations. Therefore the main aim of this thesis is to develop a formulation to account for transversely isotropic viscoelasticity in the solid phase of a biphasic material in order to capture the stress relaxation behavior of the articular cartilage under small compression with greater accuracy than the purely transversely isotropic and biphasic formulation. The principles of mathematical modeling that are going to be used to develop a new model will be explained in greater detail in the next chapter.

Another approach to simulating the mechanical behavior of a specimen is through the approach of numerical computation. Although analytical solutions are always preferable for problems (since they do not involve errors of computation such as truncation errors

or convergence issues), it is often seen that analytical solutions are feasible only for highly idealized geometries and conditions. In most cases, mechanical responses must be characterized for irregular geometries (such as an actual artificial cartilage tissue in the joint). In these scenarios, numerical approximations such as the finite element method and the finite difference method are used instead of analytically solving partial differential equations.

Numerical methods may also be used to validate existing analytical solutions. Researchers around the world have solved various geometries (such as the compression experiments) using the finite element and finite difference methods and compared them to the analytical solutions developed for them [45, 46]. Many analytical solutions are obtained by a convoluted procedure of solution (which may not exist in the time domain either) and need numerical routines just to obtain their closed form results. In such cases numerical solutions can prove to be an efficient alternative. Once validated, the researcher is free to manipulate his geometry and initial conditions without having to analytically solve the problem again.

Some notable instances of numerical modeling of compression experiments in cartilage are given below. One of the earliest implementations of the finite element method was by Spilker [47, 48] who modeled an unconfined compression experiment as well as an indentation experiment for the linear biphasic material. The advantage of using FEM here allowed the author to study the effect of friction between the rigid impermeable plates and the specimen during unconfined compressive loading (something that would be very complicated to add to the analytical formulation of the experiment). DiSilvestro re-validated Mak's biphasic and linearly viscoelastic theory using a finite element method and used it investigate various ranges of strain rates [49]. Finite elements has also proven popular for researchers who want to capture the behavior of the articular cartilage more accurately from a structural point of view. Several FEM investigations have been carried out while keeping in mind the inhomogeneities in the microstructure of cartilage (something that would be very difficult if not impossible to do analytically) such as the collagen fibrils and their orientation [50, 51, 52, 53]. Haider [54] solved the biphasic and linearly viscoelastic problem for a confined compression apparatus using

the method of finite differences and confirmed the results of the analytical solution for the same.

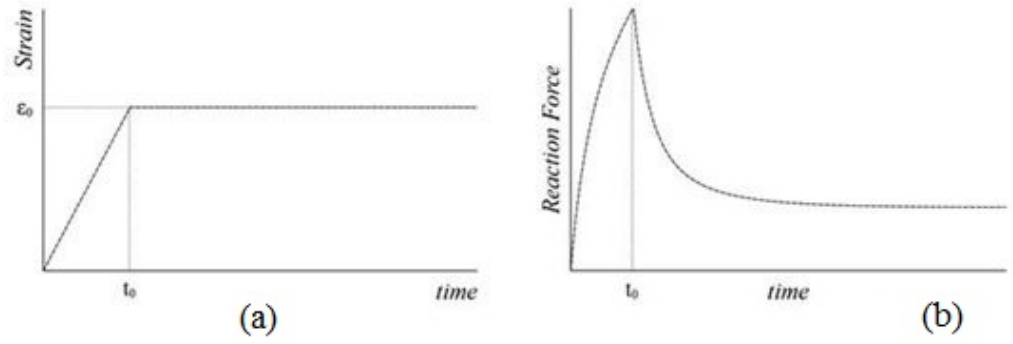

Figure 9: Fig. (a) A ramp strain (b) A stress relaxation curve

In the following discussion, the fundamentals of viscoelasticity are introduced. Viscoelasticity is defined as a phenomenon wherein a material undergoing deformation exhibits both elastic and viscous characteristics. The particular behavior of viscoelasticity we are investigating is the stress relaxation of a material on application of fixed strain. Viscous materials are seen to behave in a hereditary manner (i.e. the current state of stress or strain depends on the state of stress or strain at points of time in the past). Figure 9 shows a stress profile one might expect from the ramp strain compression of a viscoelastic material. Boltzmann (1844-1906) introduced the most general formulation for linear viscoelasticity which stated that the elongation in a specimen at any point of time is caused by the total history of loading upto that point in time and conversely that the stress in a specimen at any point of time is caused by the total history of elongation till that point of time. In a one dimensional stress relaxation case this gives us a time dependent expression of force F as-

$$F(t) = \int_0^t E(t-\tau)\frac{du(\tau)}{d\tau}d\tau \tag{1}$$

where u is the deformation in one dimension and $E(t)$ is the relaxation modulus. This

can be extended to three dimensions by -

$$\sigma_{ij}(\mathbf{X},t) = \int_{-\infty}^{t} G_{ijkl}(\mathbf{X},t-\tau)\frac{\partial \epsilon_{kl}}{\partial \tau}(\mathbf{X},\tau)d\tau \tag{2}$$

where G_{ijkl} is the fourth order relaxation tensor, ϵ_{kl} is the second order strain tensor and σ_{ij} is the second order stress tensor.

Linear viscoelasticity can also be experimentally characterized if the relaxation modulus curves corresponding to different step strains overlap (i.e. that the relaxation modulus for linear viscoelasticity is independent of step strain $E(t) = \sigma(t)/\epsilon_0$). For the new biphasic, transversely isotropic and viscoelastic constitutive model that shall be developed in the next chapter, a linearly viscoelastic formulation shall be employed.

In most examples of viscoelastic behavior, it is quite rare to get a relaxation modulus that is independent of strain [55]. In such cases, linear viscoelastic is not applicable anymore and one must look at other methods to determine the constitutive relationship of the material. One such approach is Quasi-Linear Viscoelasticity (or QLV) [56]. QLV can be characterized in a material if in a plot of log relaxation modulus versus log time, one obtains separate curves for different step strains but each curve has a similar shape. Mathematically, QLV can be represented as -

$$\sigma_{ij}(\mathbf{X},t) = \int_{\infty}^{t} G_{ijkl}(\mathbf{X},t-\tau)\frac{\partial \sigma_{kl}}{\partial \epsilon_{mn}}\frac{\partial \epsilon_{mn}}{\partial \tau}d\tau \tag{3}$$

where σ_{ij} stands for the second order stress tensor.

Equation (3) is structurally very similar to the expression for linear viscoelasticity and is thus an acceptable model for some non-linearly behaving viscoelastic materials. One must note carefully the terms within the hereditary integral for both formulations. Linear viscoelasticity depends on an infinitesimally small strain being integrated from the past whereas QLV depends on an infinitesimally small stress term being integrated from a point of time in the past. Another assumption in these formulations is that there are no jumps in stress assumed for our specimen at the start of the experiment (in that case the formulations have another term to account for the instantaneous jump in stress). In case the curves for relaxation modulus with time do not overlap or are

not similar to each other for different strain, a formulation for non-linear viscoelasticity must be chosen. Fung introduced the QLV theory for approximating the stress relaxation response of tissue such as skin, muscles, veins, tendons, ligaments etc [56].

2.4. Optimization

Once a desired constitutive model has been formulated, it must be tested against experimental data to see if it has the ability to accurately capture the behavior of the specimen. This can be said to be the second phase of a constitutive modeling project as it is during this phase that the model can be tested for its accuracy and efficiency. Feedback from this stage is used to improve the model and subsequently re-evaluate it against experimental data. In common parlance, this phase of the project is called the "curve fitting" stage where experimental data are "curve-fit" to certain material constants in the model we have developed. Curve fitting is also known as optimization which is defined as the minimization or maximization of a particular mathematical quantity. In our case, the quantity to be minimized is the error between the experimental data and the model prediction.

In the following, a short review is carried out of the major developments in optimization. Modern optimization and its origins can be traced back to the 16th century with Newton's root finding method also known as the Newton-Raphson method named after Sir Isaac Newton and Joseph Raphson which was an iterative method for finding successively better optimization of roots of a real-valued function [57]. In the mid 17th century Simpson used this iterative root finding procedure for gradient based optimization [58]. Gradient based optimization finds its logic in setting derivatives equal to zero in order to find the maxima or minima of a function. Legendre in 1807 presented the concept of least squares error reduction [59] although Gauss [60] claimed to have had knowledge of the technique earlier. Least squares reduction is the foundation of validation of mathematical models with experimental data. Cauchy in 1847 [61] formulated the sequential line search technique on a steepest descent line which involves moving in the direction of steepest descent till a minima is reached on the line before which a

new direction of steepest descent is found and the process is repeated. It adds a certain degree of heuristic control to the traditional Newton-Raphson method. In 1944, Levenberg [62] combined Cauchy's sequential line search method and Newton's method for root finding to obtain a robust optimization technique which utilizes the advantages of either method (such as Newton's method's ability to jump rather quickly to the local vicinity of an optima combined with the increased accuracy of Cauchy's sequential search in that local vicinity). This method was not prominently used until Marquardt rediscovered and popularized it [63]. In 1959, William C. Davidon presented the first Quasi-Newton method which was a modification of the well known Newton's method without the requirement to calculate Hessians for higher dimensions[64]. The Hessian matrix is a square matrix of second-order partial derivatives with respect to the dependent variables of a scalar-valued function, or scalar field. It describes the local curvature of a function of many variables. Hooke and Jeeves [65] in 1961, published their Pattern Search method for finding the minima of functions that may or may not be continuous or differentiable. This method (known as a direct search method) therefore would not need the use of gradients of the function at points and was an important advance in minimization techniques. In 1962, Spindley, Hext and Himsworth presented the Simplex search method (not to be confused with Dantzig's simplex tableu) for optimization wherein a simplex (a convex hull of n+1 vertices in n dimensions) is used to find the optima of the function by successively reducing its size[66]. Nelder and Mead [67] modified this method to account for change of size and shape (i.e. by controlling the angles of the simplex). These direct search methods were characterized by optimizers behaving in a manner such that lower values of a function were sought out at the expense of higher values. However, this caused an attraction to local minima as against the ultimate goal of finding the global optima.

Increased computing power in the late twentieth century led to the formulation of evolutionary algorithms that mimic Nature's way of finding the optimum to a particular function. When gradient based or direct search methods are unable to find the optima for complex functions, it is seen that these algorithms are capable of using their inbuilt heuristics to reach the vicinity of the optima. Some notable evolutionary algorithms are

the Particle Swarm theory [68], the Ant-Colony algorithm [69], Differential Evolution [70], the Artifical Bee Colony algorithm [71], the Cuckoo Search algorithm [72], the Bees algorithm [73], Leapfrogging [74], Harmony Search [75]. All of these algorithms are heuristic based and can be modified to aid the individual with his requirements.

Curve fits to non-linear constitutive models for mechanical behavior of materials require the use of a mechanism to minimize the difference between the experimental data and the model predicted data for parameters (which in our case are material constants). In optimization parlance a multidimensional non-linear optimization has to be carried out with the material constants as decision variables and the error between experiment and predicted values as the objective function. A convenient way to define this objective function is to use the least squares error minimization process. In this process the square of the difference of predicted model values and experimental data is minimized at each value of the time variable. In other words -

$$O.F = \sqrt{\Sigma_i \left([F_{model}(t_i) - F_{experiment}(t_i)]^2 / F_{experiment}(t_\infty)^2\right)} \tag{4}$$

One may notice in equation (4) that the squared difference of the error is normalized by the equilibrium function value for the experimental data. For stress relaxation experiments, this equilibrium value is achieved when the sample has relaxed completely. Our optimizer will then evaluate the objective function for different decision variables (in our case - these are material constants) and then obtain a set of these variables which gives us the lowest value for the objective function or in other words, the lowest error.

For curve fitting constitutive models to experimental data in the field of biomechanics, it is imperative that the global minima be reached at the end of the optimization process since the outcomes of the curve fits are material constants which characterize a particular sample being experimented. In order to ensure the global minima are reached, evolutionary swarm algorithms are generally used nowadays to curve fit the experimental data. DiSilvestro [49] and Olberding [76] used the differential evolution algorithm for curve fitting unconfined compression, indentation and confined compression data of articular cartilage. Differential evolution has emerged as the optimizer of choice for most curve fitting procedures after constitutive modeling of soft tissue in compression. Soltz

et al [43] however, used the BFGS Quasi-Newton minimization scheme (a modern descendant of Davidon's first Quasi-Newton method) to curve fit experimental data to his Conewise-Linear Elastic model for unconfined compression of cartilage. For the purpose of curve fitting, some well known evolutionary algorithms were tested for computational efficiency before Leapfrogging was finalized to curve fit our experimental data.

The studies done prior to selection of an optimizer included the test of computational efficiency in obtaining convergence. Three optimizers, differential evolution, the modified particle swarm and leapfrogging were made to optimize an objective function with the same randomized starting position of players and the time taken to reach a convergence was recorded. Our hypothesis was that leapfrogging would be a more efficient optimizer compared to differential evolution or the modified particle swarm method. There were certain reasons behind this assumption. Firstly, particle swarm and differential evolution require the selection of certain heuristic parameters by the user in order to optimise performance and these require significant trial and error. The parameters selected were on the basis of classical recommendations by the developers of these optimization algorithms and are generally not very suitable for all problems. This is not the case in leapfrogging where we rely on the inbuilt heuristic. Secondly, in every iteration of either particle swarm or differential evolution, each player is mutated and retained if it is fitter than its parent which causes a significantly higher number of function evaluations per iteration as compared to leapfrogging where only the worst player is targeted for mutation. This essentially implies that leapfrogging is focused on the elimination of the worst particle in each iteration as compared to the other two optimizers where all the players are mutated to check for a better solution (thus requiring more computational time). However, this higher degree of mutation in particle swarm and differential evolution leads to a higher probability of capturing the global optima in the same number of initializations. In Rhinehart et al [74], particle swarm was shown to reach the global optima more than twice as many times as compared to leapfrogging for the same number of random initializations for a particular function. However, since we had a good idea about the location of the global optima for our problem from reported values in literature, the exploration aspect of our optimization routine was not

very important and computational benefit took precedence over ability to obtain global optima in fewer initializations.

As shown in figure 10, Leapfrogging was able to reach convergence much more quicker than the other two optimizers for this particular problem. The convergence criteria for our study as well as subsequent model validation was given by -

$$\frac{St.Dev[X_i]}{Mean[X_i]} \leq Precision \tag{5}$$

where X_i are the values of material constants i. For example, if we are optimizing a material model with 3 parameters and our optimization routine utilizes 10 players, there are 10 particles with each having 3 material parameters and the standard deviation of the 10 values of each of the 3 material parameters divided by their mean must be less than the threshold precision for convergence. The precision value is determined by observing standard deviation values decrease to zero before deciding a magnitude to quit iterations. Other convergence criteria were also explored such as standard deviation of objective function values which was deemed unsatisfactory due to shallow optima (significant variations in parameters with low variation in objective function values near the global optima) and the standard deviation of all parameters being lower than a threshold which was rejected as it would cause an inconsistency of scale as some parameters are much larger than the others. The pseudo-code for our optimizer of choice (leapfrogging) is given in figure 11 and its corresponding Mathematica code has been provided in the appendix. The general process flow for an evolutionary algorithm is given in figure 12.

Another method of model validation is the procedure of bootstrapping [77]. Bootstrapping is carried out as a post-optimization study to ensure that the model is not sensitive to systematic deviations of experimental data. Bootstrapping uses an interpolation scheme where a certain amount of experimental data generated is averaged following which a random error is added to this average ensemble. The random error in data is calculated from residuals generated during the optimization of the generated experimental data. This extrapolated data generated from the average ensemble and the random error is then tested by multiple optimization runs (each with a different random error). If output parameters remain stable (i.e. within a certain feasible range),

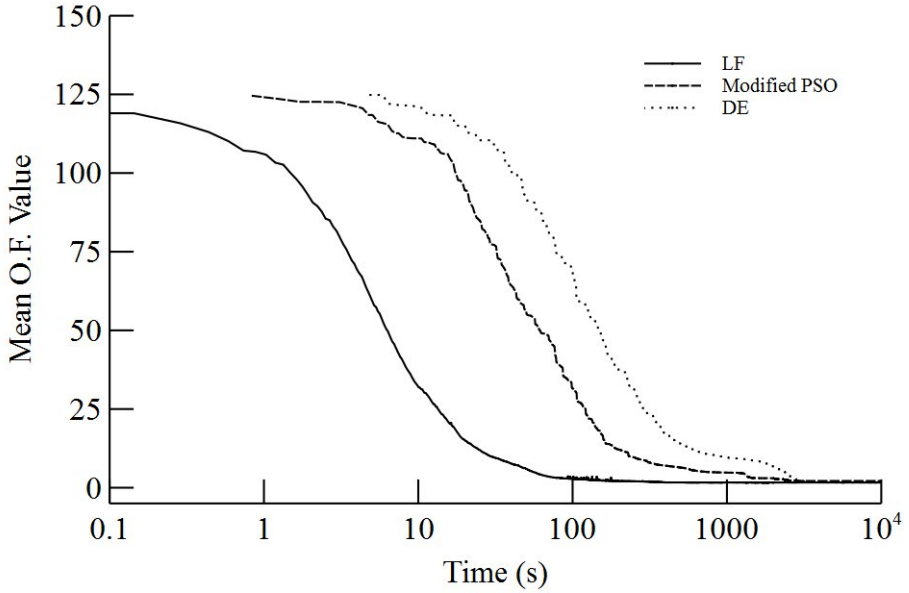

Figure 10: Convergence Studies using three optimizers - Leapfrogging - Differential Evolution - Particle Swarm

then the model is said to be insensitive to systematic errors in data.

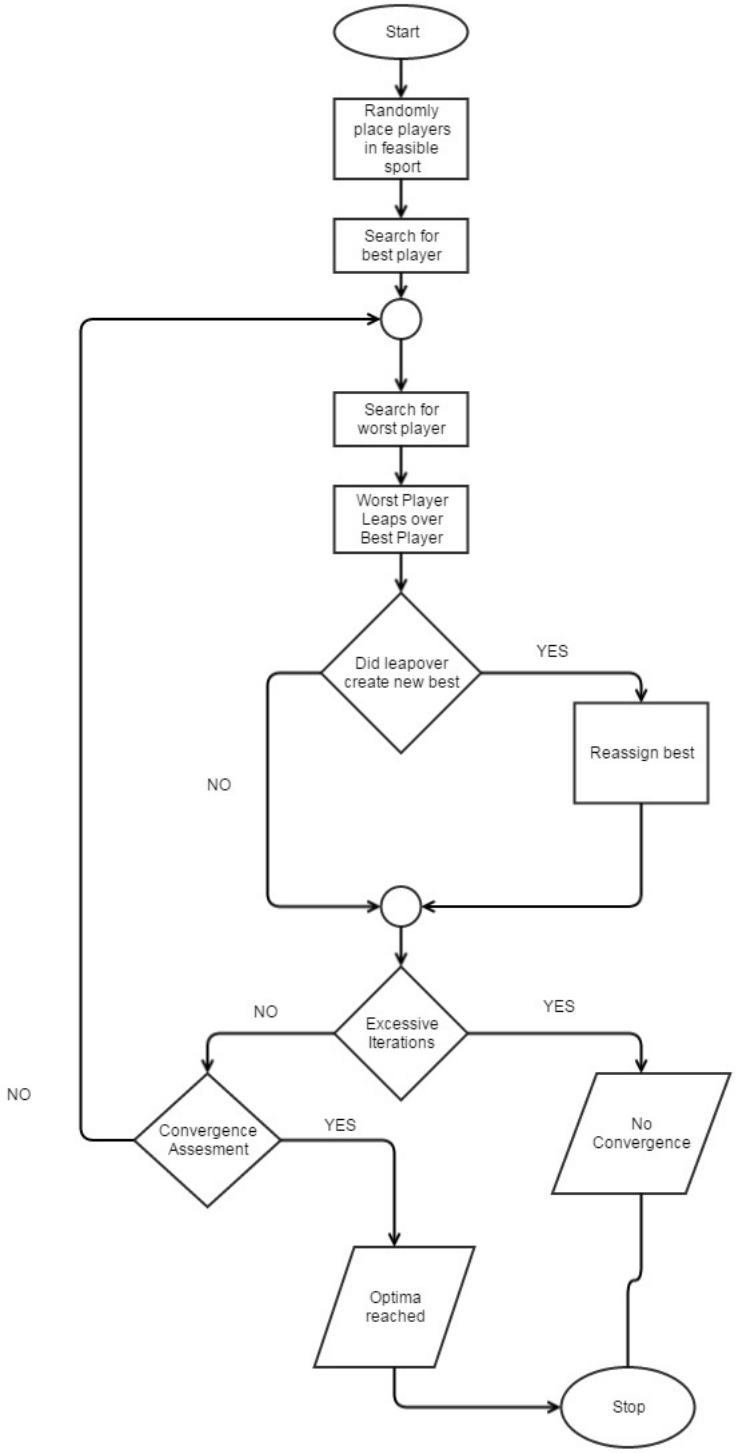

Figure 11: Pseudocode for Leapfrogging optimizer. The OF value is the error between model and experimental data. A better OF implies lower error.

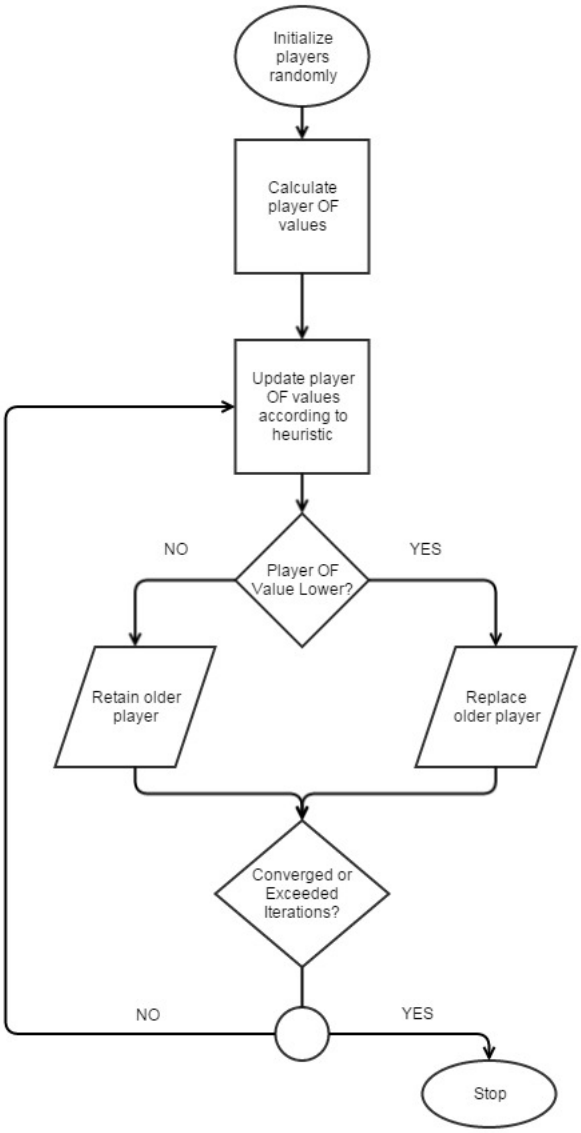

Figure 12: Process flow for general evolutionary algorithm

CHAPTER 3

Transversely Isotropic, Viscoelastic and Biphasic Model

In this chapter, a new constitutive model will be developed using some common assumptions present in literature. Our constitutive model will be developed for the unconfined compression experimental configuration (which has been discussed in extensive detail in the previous chapter). The primary assumptions we will be making in the formulation of this model is that the specimen is perfectly cylindrical, that there exists only two phases in the domain (one solid and one fluid) and that the fluid permeability is constant throughout the duration of the experiment. The other significant assumption (and the chief new component of this work) is that the solid matrix is transversely isotropic and linearly viscoelastic in nature with the plane of isotropy being in the radial direction. Before the new constitutive relationship is developed, some of the concepts behind the different relations that will be used to formulate a partial differential equation for our problem are described.

3.1. Mathematics Prerequisites

In order to set up the partial differential equation for a material and geometry, it is necessary to develop a set of governing equations. These governing equations are generated from certain relationships related to the type of analysis we are undertaking. For example, since our analysis is static in nature, the body is at a force equilibrium (not to be confused with the equilibrium stress of the experiment) throughout the duration of the experiment and throughout the volume of the specimen. A relationship can be set up to balance the different forces (due to stress, fluid pressure etc) and this will give us one of

our governing equations. These equations are also generally known as the equations of motion. In static solid mechanics, the equilibrium equations are determined by taking the divergence of the stress tensor within the body i.e. -

$$\sigma_{ij,j} = 0 \tag{6}$$

After setting up the equilibrium equations, it is important to set up the equations for local conservation of mass also knows as the continuity equations. A continuity equation describes the transport of a conserved quantity. Since mass, energy, momentum, electric charge and other natural quantities are conserved under their respective appropriate conditions, a variety of physical phenomena may be described using continuity equations. In other words, they are stronger and more localized version of the laws of conservation. Continuity equations can be expressed in integrals forms (for example in cases of flux) and in differential forms through the use of a divergence operator (which is what this formulation shall use). For our formulation, the continuity equation essentially provides us the localized version of a conservation of mass. It is given by -

$$\frac{\partial \rho}{\partial t} + (\rho v_i)_{,i} = 0 \tag{7}$$

Where ρ is the density of the material and v is the velocity vector of the material. The above equation is simplified in our formulation to account for the assumption that the density of our phases are uniform and continuity is maintained by relative motion of phases against each other. This will elaborated in the next few sections.

Once the continuity and equilibrium equations are setup, our assumptions for the constitutive relationship for the individual phases shall be substituted into them to obtain a partial differential equation.

3.2. The Biphasic Material Assumption

The linear biphasic theory states that the total tissue stress is a sum of the stresses in the solid and the liquid phase [35] -

$$\sigma_{ij}^{t} = \sigma_{ij}^{f} + \sigma_{ij}^{s} \tag{8}$$

where σ^f is the stress tensor caused due to the interstitial fluid pressure p and σ^s is the stress tensor of the solid matrix.

In the biphasic assumption the stresses developed in the solid phase are given by -

$$\sigma_{ij}^{s} = -\frac{\phi_s}{\phi_f} p\ \mathbf{I} + \sigma_{ij}^{mat} \tag{9}$$

Where σ^{mat} is the stress strain relationship for the material of the solid phase and $\mathbf{I}$ is the Identity tensor. The stresses in the fluid phase are given by the uniform radial pressure in the fluid -

$$\sigma_{ij}^{f} = -p\ \mathbf{I} \tag{10}$$

The fluid stress p used in the biphasic theory is related to the interstitial fluid pressure p_0 by the expression $p_0 = (1 + \phi_s/\phi_f)p$ [36].

Applying the conditions of equilibrium to the solid and liquid phases individually within the domain gives us -

$$\sigma_{ij,j}^{s} - K(v_i^s - v_i^f) = 0 \tag{11a}$$

$$\sigma_{ij,j}^{f} + K(v_i^s - v_i^f) = 0 \tag{11b}$$

where K is known as the diffusive resistance coefficient related to the tissue permeability k by $K = \phi_f^2/k$. The above equations reflect the assumption that the relative motion between the phases causes a transfer of linear momentum between them to ensure equilibrium. On addition of the the equations we recover the equilibrium condition

of the entire domain -

$$\sigma^t_{ij,j} = 0 \tag{12}$$

Now that the equilibrium equations are ready, continuity conditions must be set up for the biphasic assumption. A primary assumption made about the two phases in the biphasic material is that both phases are intrinsically incompressible. This leads to the understanding that the solid matrix can only move in to occupy a certain volume of the domain if an equal an opposite amount of fluid is squeezed out of it. This phenomenon, coupled with the fact that both phases are homogeneous (ρ is constant for both of them) gives us -

$$\phi_f v^f_{i,i} + \phi_s v^s_{i,i} = 0 \tag{13}$$

Taking the advantage of the geometry of the sample used for this experiment, the formulation uses the cylindrical coordinates system which helps us write equation (13) as -

$$\phi_f \left(\frac{\partial v^f_r}{\partial r} + \frac{v^f_r}{r} + \frac{\partial v^f_z}{\partial z} \right) + \phi_s \frac{\partial}{\partial t} \left(\frac{\partial u}{\partial r} + \frac{u}{r} + \epsilon(t) \right) = 0 \tag{14}$$

An important assumption made here is that due to assumption of infinitesimal deformation $v^s_{i,i} \approx \frac{\partial}{\partial t}(u^s_i)$. Also, u implies displacement of the solid matrix in the radial direction and $\epsilon(t) = \partial u^s_z/\partial t$. It is assumed that solid-fluid relative motion exists only in the $r - \theta$ plane which gives us $v^f_z = v^s_z = \partial u^s_z/\partial t$ from which we get $\partial v^f_z/\partial z = \partial \epsilon/\partial t$ where ϵ is the axial strain $\partial u^s_z/\partial z$. It is noted here that there is no fluid or solid phase motion in the θ direction.

The above equation is integrated with respect to r with the condition that $v^f_r = 0$ at $r = 0$ to give -

$$v^f_r = -\frac{\phi_s}{\phi_f}\frac{\partial u}{\partial t} - \frac{r}{2}\left(1 + \frac{\phi_s}{\phi_f}\right)\frac{\partial \epsilon}{\partial t} \tag{15}$$

Now our governing equations are all set up. We proceed to eliminate the fluid stress

p from the equations of equilibrium (equation 11a and 11b) by using equations (9,10) and use our continuity relation (equation 15) to obtain -

$$(\nabla.\sigma^{mat})_r = \frac{1}{k}\left(\frac{\partial u}{\partial t} + \frac{r}{2}\frac{\partial \epsilon}{\partial t}\right) \tag{16}$$

The left hand side of the above equation symbolizes the radial component of the divergence of the second order solid phase stress tensor in cylindrical coordinates. It is assumed that there is no shearing in this experimental configuration. The above equation symbolizes the principle partial differential equation for radial displacement in the biphasic problem.

For determining the axial force intensity in the biphasic problem, a fluid pressure field also needs to be determined. We can obtain a partial differential equation for the fluid pressure from putting equation (15) into (11b) and noting the relation between the diffusive resistivity coefficient K and the fluid permeability k -

$$(1 + \frac{\phi_s}{\phi_f})\frac{\partial p}{\partial r} = \frac{1}{k}\left(\frac{\partial u}{\partial t} + \frac{r}{2}\frac{\partial \epsilon}{\partial t}\right) \tag{17}$$

which simplifies to -

$$\frac{\partial p_0}{\partial r} = \frac{1}{k}\left(\frac{\partial u}{\partial t} + \frac{r}{2}\frac{\partial \epsilon}{\partial t}\right) \tag{18}$$

Both relations for radial displacement (equation 16) and pressure (equation 18) are solved analytically (if possible) and used in the following relation to determine the axial load intensity (i.e. the load per unit undeformed area)-

$$f(t) = \int_0^{r_0} \sigma_{zz}^t(t) 2\pi r dr / \pi r_0^2 \tag{19}$$

The relation shown above integrates the axial stress by summing up infinitesimally thin radial strips from the center to the radius of the specimen to obtain the average force on the specimen which is then divided by the area of the specimen at the start of

the experiment. The axial stress σ_{zz} is the total stress in the specimen given by -

$$\sigma^t_{zz} = -(1 + \frac{\phi_s}{\phi_f})p_{zz} + \sigma^{mat}_{zz} = -(p_0)_{zz} + \sigma^{mat}_{zz} \tag{20}$$

The above relation can be obtained by summing up the equations (9 and 10).

In addition to the main partial differential equations, certain boundary conditions are also assumed for the unconfined compression problem where for $r = 0$, in order to account for zero radial displacement at the centre of the specimen we have -

$$u = 0 \tag{21}$$

and for $r = r_0$ (r_0 is specimen radius) in order to account for zero traction on the lateral surface of the specimen -

$$\sigma_{rr} = 0 \tag{22}$$

For fluid pressure our boundary conditions are defined by a pressure free lateral surface -

$$p(r_0, t) = 0 \tag{23}$$

The initial conditions (i.e. at time $t = 0$) for the unconfined compression experiment are given by -

$$u = 0 \text{ and } p = 0 \tag{24}$$

3.3. Solid Phase Constitutive Relationship

In this section we shall discuss the mathematical relationship used to describe the stress strain behavior of the solid phase of the biphasic domain. First we shall take a look at

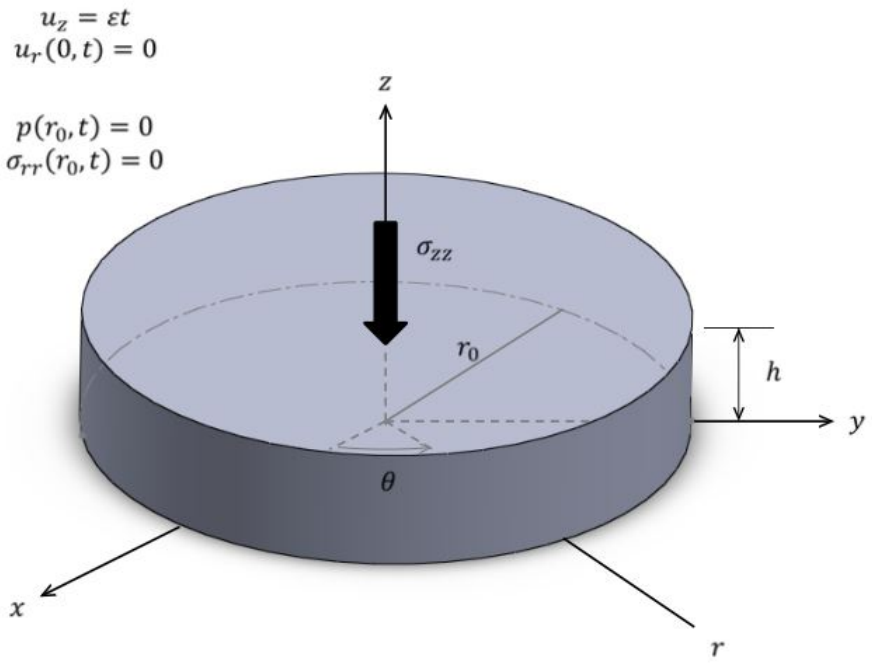

Figure 13: Unconfined Compression Sample Geometry

Cohen's model which has a transversely isotropic solid phase (with no added viscoelasticity). The stress strain relationships developed here will form the foundation of the complexity we wish to introduce later.

For an elastic solid matrix with transverse isotropy we have -

$$\begin{pmatrix} \sigma_{rr} \\ \sigma_{\theta\theta} \\ \sigma_{zz} \\ \sigma_{zr} \end{pmatrix} = \begin{pmatrix} C_{11} & C_{12} & C_{13} & 0 \\ C_{12} & C_{11} & C_{13} & 0 \\ C_{13} & C_{13} & C_{33} & 0 \\ 0 & 0 & 0 & C_{44} \end{pmatrix} \begin{pmatrix} \epsilon_{rr} \\ \epsilon_{\theta\theta} \\ \epsilon_{zz} \\ 2\epsilon_{zr} \end{pmatrix} \tag{25}$$

where (r, θ, z) are the cylindrical coordinates and the $r - \theta$ plane is the plane of isotropy. The five independent parameters of transverse isotropy are then given in terms of moduli and Poisson's ratios in the plane of isotropy and in a direction perpendicular to it.

$$C_{11} = \frac{E_1(1 - \nu_{31}^2 E_1/E_3)}{(1 + \nu_{21})\Delta_1} \tag{26}$$

$$C_{12} = \frac{E_1(\nu_{21} - \nu_{31}^2 E_1/E_3)}{(1 + \nu_{21})\Delta_1} \tag{27}$$

$$C_{13} = \frac{E_1 \nu_{31}}{\Delta_1} \tag{28}$$

$$C_{33} = E_3[1 + 2\nu_{31}^2 (E_1/E_3)/\Delta_1] \tag{29}$$

$$C_{44} = G_{31} \tag{30}$$

where $E_1, \nu_{21} = \nu_{12}$ and $E_3, \nu_{31} = \nu_{13} E_3/E_1$ are the modulus and Poisson ratio in the transverse plane and plane perpendicular to plane of isotropy respectively. G_{31} is the out of plane shear modulus and $\Delta_1 = 1 - \nu_{21} - 2\nu_{31}^2 E_1/E_3$.

From the above relations we obtain (noting that $\epsilon_{rr} = \partial u/\partial r$, $\epsilon_{\theta\theta} = u/r$) -

$$\sigma_{rr} = C_{11}\frac{\partial u}{\partial r} + C_{12}\frac{u}{r} + C_{13}\epsilon_{zz} \tag{31}$$

$$\sigma_{\theta\theta} = C_{12}\frac{\partial u}{\partial r} + C_{11}\frac{u}{r} + C_{13}\epsilon_{zz} \tag{32}$$

The radial component of the divergence of the second order stress tensor describing the solid phase constitutive relationship in polar coordinates for the unconfined compression experiment is given by -

$$(\nabla . \sigma^{mat})_r = \frac{\partial \sigma_{rr}}{\partial r} + \frac{1}{r}(\sigma_{rr} - \sigma_{\theta\theta}) \tag{33}$$

Which ends up giving us -

$$(\nabla.\sigma^{mat})_r = C_{11}\left(\frac{\partial^2 u}{\partial r^2} + \frac{1}{r}\frac{\partial u}{\partial r} - \frac{u}{r^2}\right) \tag{34}$$

This equation may then be combined with the general biphasic partial differential equation for the radial displacement (equation 16) to completely describe the radial displacement of the specimen in the unconfined compression experiment as shown below -

$$C_{11}\frac{\partial^2 u}{\partial r^2} + C_{11}\frac{1}{r}\frac{\partial u}{\partial r} - C_{11}\frac{u}{r^2} = \frac{1}{k}\{\frac{\partial u}{\partial t} + \frac{r}{2}\frac{\partial \epsilon}{\partial t}\} \tag{35}$$

The above equation can be solved for the radial displacement of the solid phase (u) by normalizing all our variables and moving the relation to the frequency domain. This shall be explained in further detail during the solution of our proposed formulation in section 3.5.

3.4. Incorporating Linear Viscoelasticity to Solid Phase

Linear viscoelasticity has been covered in detail in the chapter 2 and it is incorporated into the stress strain relationship in the following manner. Using Voigt notation, we have defined a time dependent stiffness parameter for our solid phase given by -

$$C_{ij}(t) = C_{ij}g(t) \tag{36}$$

Where the relaxation function $g(t)$ is defined as -

$$g(t) = \{1 + \int_0^t \frac{H(\tau)}{\tau} e^{-t/\tau} d\tau\} \tag{37}$$

and $H(\tau)$ is the relaxation spectrum of choice for this model. The most commonly

chosen form for the relaxation spectrum has been specified by the box spectrum [78] -

$$H(\tau) = \begin{cases} c & \tau_1 \leq \tau \leq \tau_2 \\ 0 & \tau < \tau_1 \ \& \ \tau > \tau_2 \end{cases} \tag{38}$$

In the above expression, c is a dimensionless constant and τ_1, τ_2 are constants having the dimensions of time and defining the period of time during which a linearly viscoelastic relationship is in place. We introduce a convolution integral relationship between the time dependent stiffness parameter given by -

$$C_{ij}\epsilon^* = \int_0^t C_{ij}(t-\tau)\frac{\partial \epsilon}{\partial \tau}d\tau \tag{39}$$

Furthermore, we assume a time dependent constitutive relationship between the stiffness matrix parameter and the strain. For the radial stress we have -

$$\sigma_{rr} = C_{11}\frac{\partial u^*}{\partial r} + C_{12}\frac{u^*}{r} + C_{13}\epsilon^*_{zz} \tag{40}$$

where radial, axial and circumferential strains have their usual expressions in polar coordinates. Similarly, for the circumferential stress -

$$\sigma_{\theta\theta} = C_{12}\frac{\partial u^*}{\partial r} + C_{11}\frac{u^*}{r} + C_{13}\epsilon^*_{zz} \tag{41}$$

where u and r are the radial displacement and distance respectively.

On using the expression for radial and circumferential stress given by equations (40) and (41) in equations (33) and (16) we can obtain -

$$C_{11}\frac{\partial^2 u^*}{\partial r^2} + C_{11}\frac{1}{r}\frac{\partial u^*}{\partial r} - C_{11}\frac{u^*}{r^2} = \frac{1}{k}\{\frac{\partial u}{\partial t} + \frac{r}{2}\frac{\partial \epsilon}{\partial t}\} \tag{42}$$

A Laplace transform of equation (42) gives us -

$$C_{11}\bar{g}\frac{\partial^2\bar{u}}{\partial r^2} + C_{11}\bar{g}\frac{1}{r}\frac{\partial\bar{u}}{\partial r} - C_{11}\bar{g}\frac{\bar{u}}{r^2} = \frac{1}{k}\{s\bar{u} + \frac{r}{2}s\bar{\epsilon}\} \tag{43}$$

where $\bar{g} = 1 + c\log(\frac{1+s\tau_2}{1+s\tau_1})$. The above relation is then normalized by the relations $\acute{u} = u/r_0$ and $\acute{r} = r/r_0$, to give us -

$$\{\frac{\partial^2\bar{\acute{u}}}{\partial\bar{\acute{r}}^2} + \frac{1}{\bar{\acute{r}}}\frac{\partial\bar{\acute{u}}}{\partial\bar{\acute{r}}} - \frac{\bar{\acute{u}}}{\bar{\acute{r}}^2}\} - f\bar{\acute{u}} = \frac{\bar{\epsilon}\bar{\acute{r}}}{2}f \tag{44}$$

Here we have defined a term -

$$f = \frac{r_0^2 s}{C_{11}\ k\ \bar{g}} \tag{45}$$

where r_0 has been defined previously as the radius of the cartilage specimen and s is the Laplace transform parameter.

Our problem has now been defined in its entirety. Our aim is to solve equation (44) using the normalized and Laplace transformed versions of the boundary conditions stated in equations (21 and 22).

3.5. Solution of New Partial Differential Equations

The newly formulated PDE for the radial displacement (equation 44) in our unconfined compression experiment can be compared to the general form of the modified Bessel Differential Equation -

$$r^2\frac{\partial^2 u}{\partial r^2} + r\frac{\partial u}{\partial r} - (\lambda^2 r^2 + \nu^2)u = 0 \tag{46}$$

The solution to the modified Bessel Differential equation is given by -

$$u = L_1 I_1[\lambda r] + L_2 K_1[\lambda r] \tag{47}$$

Where L_1 and L_2 are constants and I_1 and K_1 are Bessel Functions of the first and second kind with order 1 respectively. It is to be noted here that as $r \to 0, K_1 \to \infty$ therefore to accommodate our solution the term L_2 is to be taken as zero. Therefore the general solution for our problem is given by -

$$\bar{\acute{u}} = L_1 I_1[\lambda \acute{r}] \tag{48}$$

In order to complete our solution we need to determine a particular solution to our problem. It is seen that on choosing a particular function of $-\frac{\bar{\epsilon}\acute{r}}{2}$, equation (44) is satisfied. This gives us a final solution form of -

$$\bar{\acute{u}} = L_1 I_1[\lambda \acute{r}] - \frac{\bar{\epsilon}\acute{r}}{2} \tag{49}$$

We can now substitute the above relation into the boundary condition for zero radial stress on the lateral sides of the specimen to obtain a value for L_1. The final solution for $\bar{u}$ (now dimensionalized) is given by -

$$\bar{u} = r_0 \frac{\bar{\epsilon}}{2} \frac{(C_{11} + C_{12} - 2C_{13}) I_1[\sqrt{f} r / r_0]}{C_{11}\sqrt{f} I_0[\sqrt{f}] - I_1[\sqrt{f}](C_{11} - C_{12})} - \frac{\bar{\epsilon} r}{2} \tag{50}$$

Now that we have obtained a solution for the radial displacement we can use it to solve for the fluid pressure distribution in the radial direction. On taking a laplace transform of equation (18) and performing some rearrangement of terms we obtain -

$$\bar{p_0} = -\frac{1}{k} \int_r^{r_0} [s\bar{u} + sr\bar{\epsilon}/2]\, dr \tag{51}$$

Substituting equation (50) into (51) and integrating gives us the solution for the fluid pressure distribution in the specimen -

$$\bar{p_0} = \frac{C_{11}}{2} \bar{g} \sqrt{f} \bar{\epsilon} \frac{(C_{11} + C_{12} - 2C_{13})\{I_0[\sqrt{f} r / r_0] - I_0[\sqrt{f}]\}}{C_{11}\sqrt{f} I_0[\sqrt{f}] - I_1[\sqrt{f}](C_{11} - C_{12})} \tag{52}$$

Using equations (50) and (52) in the Laplace transformed version of equation (19) will give us the final expression for axial load intensity. The Laplace transformed version

of equation (19) is given by -

$$\bar{f} = \frac{2}{r_0^2}\int_0^{r_0}\left[-\bar{p_0} + C_{13}\bar{g}\left(\frac{\partial \bar{u}}{\partial r} + \frac{\bar{u}}{r}\right) + C_{33}\bar{\epsilon}\bar{g}\right] r\ dr \tag{53}$$

where $\bar{g} = 1 + c\log(\frac{1+s\tau_2}{1+s\tau_1})$ is the Laplace transform of the relaxation function. On substituting our equations for $\bar{u}$ and $\bar{p}$ into the above equation and integrating we obtain -

$$\bar{f} = \frac{C_{11} - C_{12}}{2}\frac{C_1 I_0[\sqrt{f}] - C_2 C_0 \frac{I_1(\sqrt{f})}{\sqrt{f}}}{I_0\sqrt{f} - C_0\frac{I_1\sqrt{f}}{\sqrt{f}}}\{1 + c\log(\frac{1+s\tau_2}{1+s\tau_1})\}\bar{\epsilon} \tag{54}$$

where -

$$C_0 = \frac{C_{11} - C_{12}}{C_{11}},\quad C_1 = \frac{2C_{33} + C_{11} + C_{12} - 4C_{13}}{C_{11} - C_{12}}, \tag{55}$$
$$C_2 = \frac{C_{33}(C_{11} - C_{12}) + C_{11}(C_{11} + C_{12} - 4C_{13}) + 2C_{11}^2}{(C_{11} - C_{12})^2}$$

This equation can be inverted to the time domain through a numerical inversion routine. We have used the De Hoog algorithm [79] to invert this expression from the frequency domain as it does a fairly robust and computationally inexpensive job of the inversion. However slight errors were noticed near the discontinuities of the inverted function (near the peak stress). The Laplace inversion routine used to obtain the axial force intensity has been included in the appendix.

3.6. Selective Viscoelasticity in Radial and Axial Directions

With the assumption that $\nu_{13} = 0$ we have the following simplifications of the stiffness matrix parameters-

$$C_{11} = \frac{E_1}{(1 + \nu_{21}\Delta_1)}\ , C_{12} = \frac{E_1\nu_{21}}{(1 + \nu_{21}\Delta_1)}\ , C_{13} = 0, C_{33} = E_3 \tag{56}$$

with $\Delta_1 = 1 - \nu_{21}$. Under this condition, the only parameters contributing to viscoelasticity in the radial and axial directions are the moduli in those directions respectively. With this knowledge we can then construct simplifications of (54) for cases in which E_3 may or may not be viscoelastic. The axial force intensity reduces to -

$$\bar{f} = \frac{2}{r_0^2} \int_0^{r_0} [-\bar{p} + E_3 \bar{\epsilon} \bar{g}] \, r \, dr \tag{57}$$

in case of E_3 being viscoelastic and incase only E_1 is assumed to be viscoelastic we get -

$$\bar{f} = \frac{2}{r_0^2} \int_0^{r_0} [-\bar{p} + E_3 \bar{\epsilon}] \, r \, dr \tag{58}$$

Note the absence of the $\bar{g}$ term in the relationship above.

3.7. Investigation of Proposed Model

In order to capture the behavior of the proposed model to the influence of various parameters, a parametric study was employed. This study was carried out by varying various parameters within acceptable ranges of deviation. The elastic and biphasic parameters were obtained from Cohen et al [6] ($E_1 = 4.55$ MPa, $E_3 = 0.47$ MPa, $k = 5\text{x}10^{-15}$ $\text{m}^4/\text{N.s}$, $\nu_{21} = 0.3$, $\nu_{31} = 0$) and the viscoelastic parameters were obtained from Setton et al [80] ($c = 0.16$, $\tau_1 = 0.06$s, $\tau_2 = 201$s). These parameters were varied and their effects were recorded on the axial load intensity with time. Inferences were then drawn about the effect of each parameter on a simulated unconfined compression experiment. The parametric studies were carried out for both versions of our proposed formulation with viscoelasticity in all directions and in only direction as discussed in the previous section. After these parametric studies were concluded, optimization algorithms were used to curve fit experimental data to our proposed formulation.

As shown in figure 14 and 15 the increased duration of ramp led to a lower peak stress reached but had virtually no effect on the equilibrium stress in the specimen.

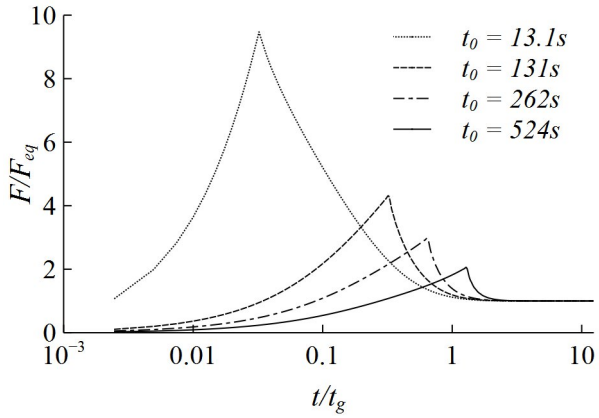

Figure 14: Effect of Ramptime - Viscoelasticity in all directions. Model Parameters : $E_1 = 4.55$ MPa, $E_3 = 0.47$ MPa, $\nu_{21} = 0.3$, $\nu_{31} = 0$, $k = 5\text{x}10^{-15}$, $c = 0.16$, $\tau_1 = 0.06$s, $\tau_2 = 201$s, radius = 6.35mm, 10% strain

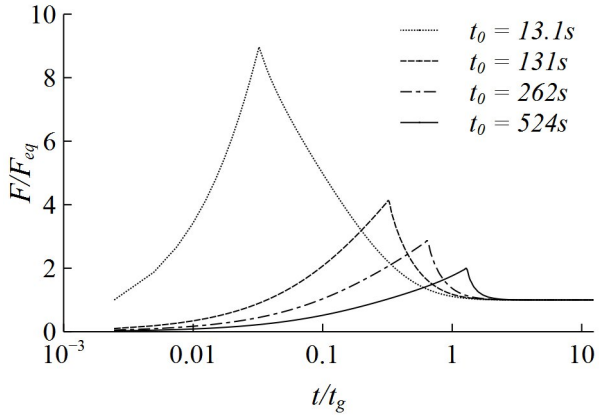

Figure 15: Effect of Ramptime - Viscoelasticity in E_1 direction. Model Parameters : $E_1 = 4.55$ MPa, $E_3 = 0.47$ MPa, $\nu_{21} = 0.3$, $\nu_{31} = 0$, $k = 5\text{x}10^{-15}$, $c = 0.16$, $\tau_1 = 0.06$s, $\tau_2 = 201$s, radius = 6.35mm, 10% strain

It was inferred that a slower ramp caused a large amount of relaxation during the strain ramping itself which prevents a high peak stress being reached. Higher strain rates would thus cause higher stresses. However equilibrium stress would naturally stay constant since viscoelasticity had no effect to play on its magnitude.

The viscoelastic parameter c was responsible for controlling the peak of the axial force intensity and also played a part in the curvature of the subsequent relaxation as shown

in Figure 16. Equilibrium stresses were not affected by this parameter as expected. For the second version of the formulation with only E_1 viscoelastic, a lower effect on the peak stress was seen although a significant effect on the ramp and relaxation curvature remained as shown in figure 17. This observation followed the general observations of the scientific community about the behavior of c [38].

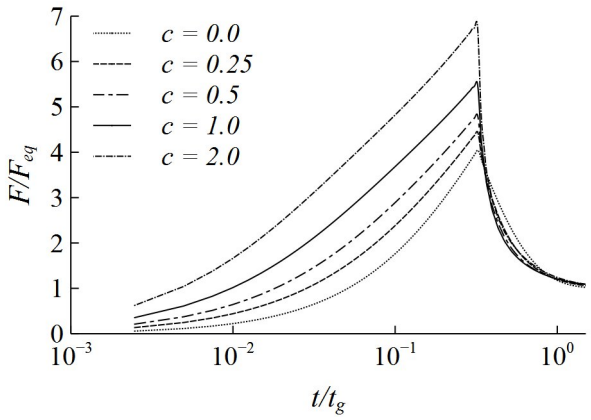

Figure 16: Effect of c - Viscoelasticity in all directions. Model Parameters : $E_1 = 4.55$ MPa, $E_3 = 0.47$ MPa, $\nu_{21} = 0.3$, $\nu_{31} = 0$, $k = 5\text{x}10^{-15}$, ramp time = 131s, $\tau_1 = 0.06$s, $\tau_2 = 201$s, radius = 6.35mm, 10% strain

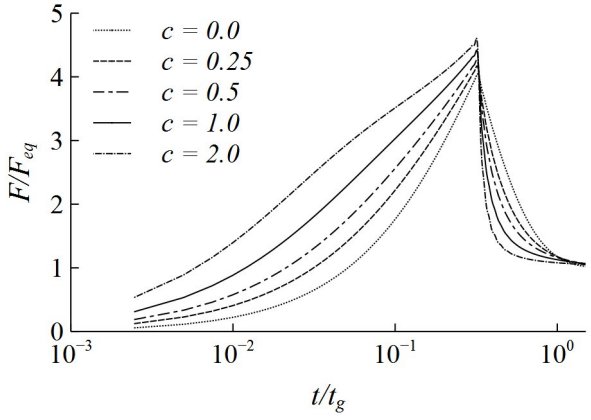

Figure 17: Effect of c - Viscoelasticity in E_1 direction. Model Parameters : $E_1 = 4.55$ MPa, $E_3 = 0.47$ MPa, $\nu_{21} = 0.3$, $\nu_{31} = 0$, $k = 5\text{x}10^{-15}$, ramp time = 131s, $\tau_1 = 0.06$s, $\tau_2 = 201$s, radius = 6.35mm, 10% strain

At ranges of c lower than one, the effect of τ_1 was seen to be negligible as seen in

the figure 18. This was also the case for the second version of the formulation. The ranges for τ_1 were chosen in accordance with literature where it is seen that their values are very rarely above 1s. In addition, the effect of τ_1 at different ranges of the other parameters were also examined.

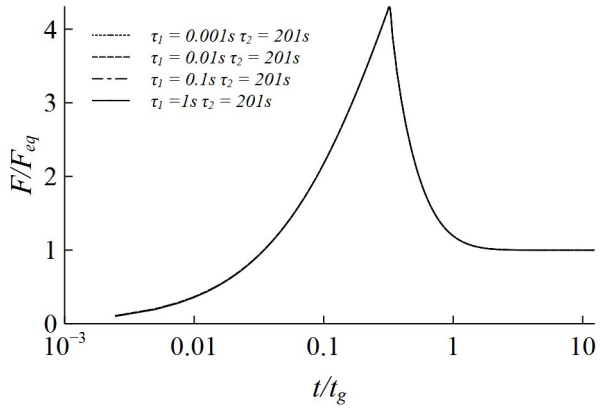

Figure 18: Effect of τ_1 - Viscoelasticity in all directions. Model Parameters : $E_1 = 4.55$ MPa, $E_3 = 0.47$ MPa, $\nu_{21} = 0.3$, $\nu_{31} = 0$, $k = 5\text{x}10^{-15}$, ramp time = 131s, $c = 0.16$, τ_2 = 201s, radius = 6.35mm, 10% strain

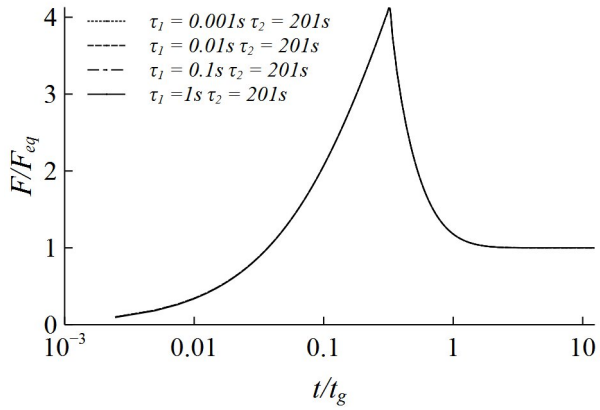

Figure 19: Effect of τ_1 - Viscoelasticity in E_1 direction. Model Parameters : $E_1 = 4.55$ MPa, $E_3 = 0.47$ MPa, $\nu_{21} = 0.3$, $\nu_{31} = 0$, $k = 5\text{x}10^{-15}$, ramp time = 131s, $c = 0.16$, τ_2 = 201s, radius = 6.35mm, 10% strain

Increasing τ_2 showed an increased peak stress developed within the range of simulation. An interesting feature of τ_2 was the lack of effect on equilibrium stress. Infact

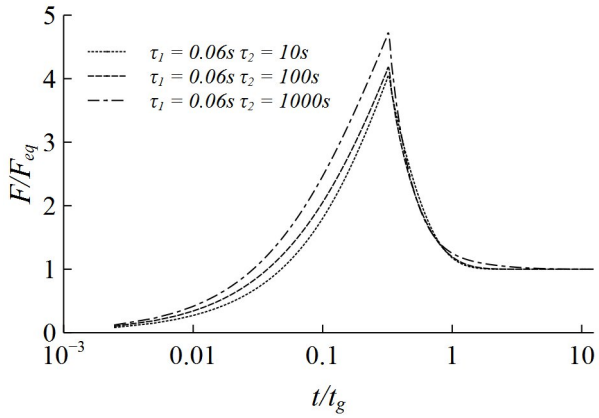

Figure 20: Effect of τ_2 - Viscoelasticity in all directions. Model Parameters : $E_1 = 4.55$ MPa, $E_3 = 0.47$ MPa, $\nu_{21} = 0.3$, $\nu_{31} = 0$, $k = 5\text{x}10^{-15}$, ramp time = 131s, $c = 0.16$, τ_1 = 0.06s, radius = 6.35mm, 10% strain

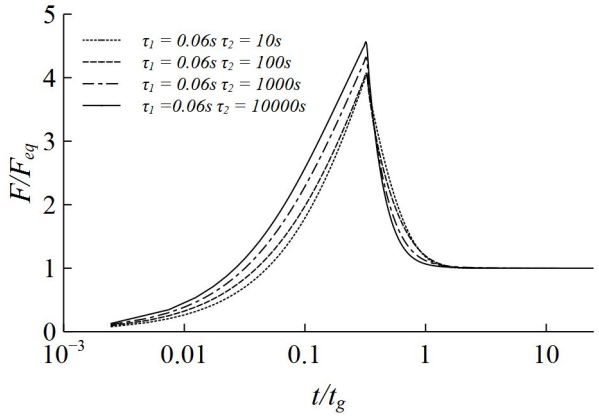

Figure 21: Effect of τ_2 - Viscoelasticity in E_1 direction. Model Parameters : $E_1 = 4.55$ MPa, $E_3 = 0.47$ MPa, $\nu_{21} = 0.3$, $\nu_{31} = 0$, $k = 5\text{x}10^{-15}$, ramp time = 131s, $c = 0.16$, τ_1 = 0.06s, radius = 6.35mm, 10% strain

the non-effect of viscoelastic parameters on the equilibrium stress backs up the general observation of equilibrium stress being dependent on E_3 only. It could be definitively concluded that the peak stress, ramp and relaxation curvature were affected the most by τ_2 & c amongst the viscoelastic parameters.

For a transversely isotropic material such as the one we have assumed for our formulation, there are two Poisson's ratios. The in-plane Poisson's ratio is ν_{21} and for

several purposes is fixed at 0.49 [5] (for example during optimization). The out of plane Poisson's ratio is ν_{31} and is generally fixed at zero in order to ensure that equilibrium conditions for stress in the unconfined and confined compression experiments (which are observed to be similar in the experimental setup) are seen to match from a theoretical point of view [6]. Varying the in plane Poisson's ratio caused an increased peak stress and a variation of the ramp curvature. The relaxation curvature and the equilibrium stress were not affected as shown in figures 22 & 23.

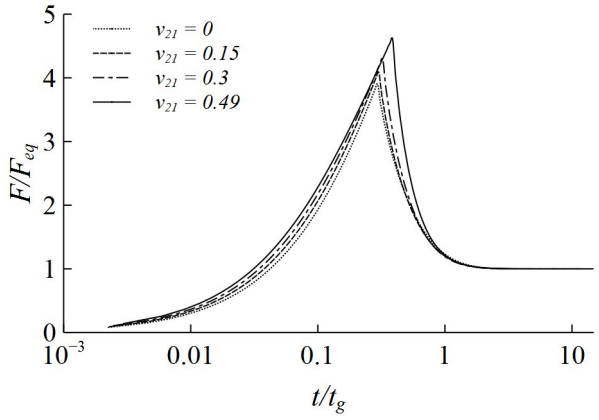

Figure 22: Effect of ν_{21} - Viscoelasticity in all directions. Model Parameters : $E_1 = 4.55$ MPa, $E_3 = 0.47$ MPa, $\nu_{31} = 0$, $k = 5\text{x}10^{-15}$, ramp time = 131s, $c = 0.16$, $\tau_1 = 0.06$s,τ_2 = 201s, radius = 6.35mm, 10% strain

In order to analyze the effect of ν_{31} it was necessary to explore ranges for this parameter that did not violate any physical properties of the model. For example the set of parameters chosen for the simulation could not lead to any term in the formulation being zero or negative. For this reason the range of ν_{31} was limited from 0.0 to 0.14. In case of the E_1 viscoelastic version of the formulation, it is a necessary condition to keep ν_{31} fixed at zero. For the version with viscoelasticity present in all directions, increased ν_{31} was seen to decrease the peak stress without causing any effect on the equilibrium stress.

The fluid permeability parameter k controls the fluid dependent stress relaxation of the formulation. Increasing the parameter was seen to have a reduction in the peak stress as shown in figures 25 and 26. A similar behavior was observed for the second

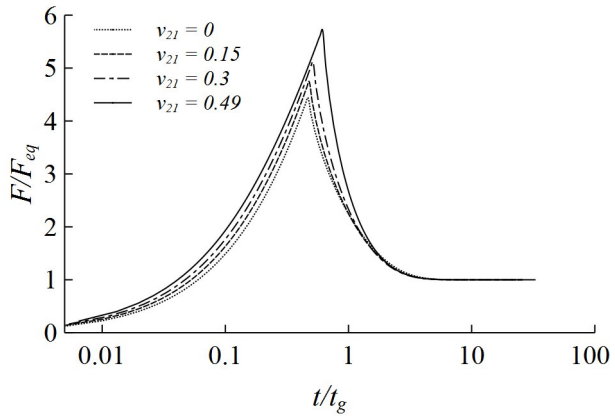

Figure 23: Effect of ν_{21} - Viscoelasticity in E_1 direction. Model Parameters : $E_1 = 4.55$ MPa, $E_3 = 0.47$ MPa, $\nu_{31} = 0$, $k = 5\text{x}10^{-15}$, ramp time = 131s, $c = 0.16$, $\tau_1 = 0.06$s,$\tau_2 = 201$s, radius = 6.35mm, 10% strain

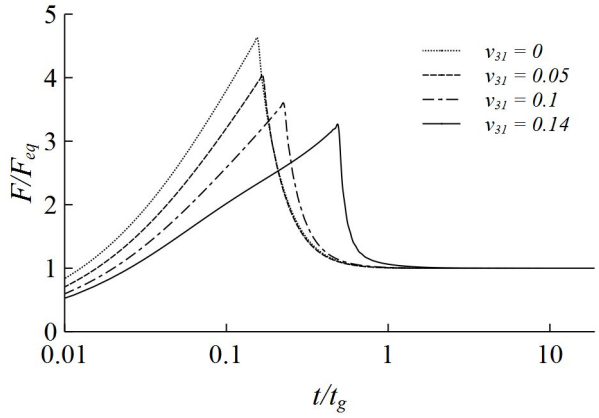

Figure 24: Effect of ν_{31} - Viscoelasticity in all directions. Model Parameters : $E_1 = 4.55$ MPa, $E_3 = 0.47$ MPa, $\nu_{21} = 0.49$, $k = 5\text{x}10^{-15}$, ramp time = 131s, $c = 0.16$, $\tau_1 = 0.06$s, $\tau_2 = 201$s, radius = 6.35mm, 10% strain

version of the formulation. The similarity of response in both the versions indicates that the fluid permeability affects the behavior of the formulation independent of solid phase viscoelasticity.

Increasing the ratio of E_1/E_3 caused an increase in the peak stress of the simulated specimen. Equilibrium was not affected by the ratio. The same behavior was observed for both versions of the new formulation. This was in accordance with the general under-

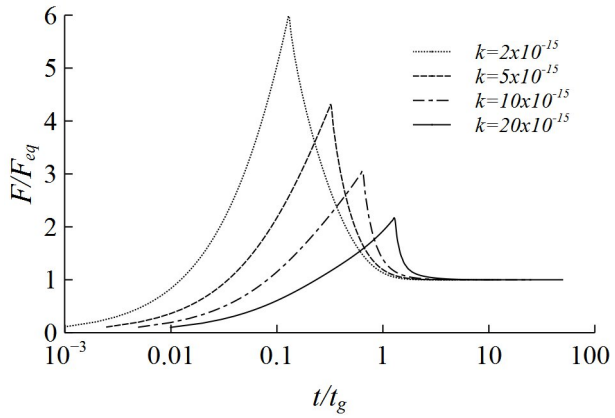

Figure 25: Effect of κ - Viscoelasticity in all directions. Model Parameters : $E_1 = 4.55$ MPa, $E_3 = 0.47$ MPa, $\nu_{21} = 0.49$, $\nu_{31} = 0.0$, ramp time = 131s, $c = 0.16$, $\tau_1 = 0.06$s, $\tau_2 = 201$s, radius = 6.35mm, 10% strain

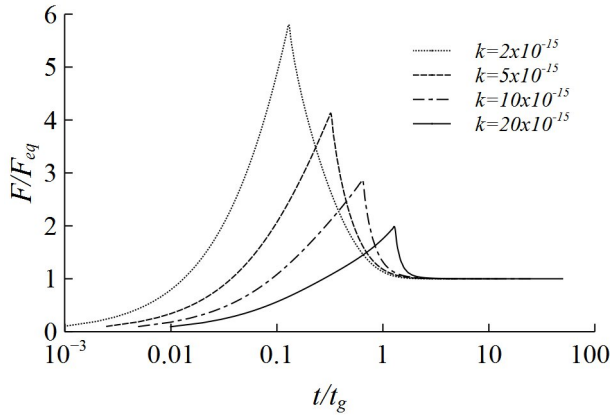

Figure 26: Effect of κ - Viscoelasticity in E_1 direction. Model Parameters : $E_1 = 4.55$ MPa, $E_3 = 0.47$ MPa, $\nu_{21} = 0.49$, $\nu_{31} = 0.0$, ramp time = 131s, $c = 0.16$, $\tau_1 = 0.06$s, $\tau_2 = 201$s, radius = 6.35mm, 10% strain

standing of the biphasic formulation in unconfined compression where a higher moduli of the material in the radial direction would cause a more significant force gradient with time during the ramp.

Reducing the radius caused a reduction in the peak stress developed. Equilibrium stresses were not affected. In the purpose of our investigations we also found that the radius affected the parameter kappa significantly during the curve fitting procedure. It

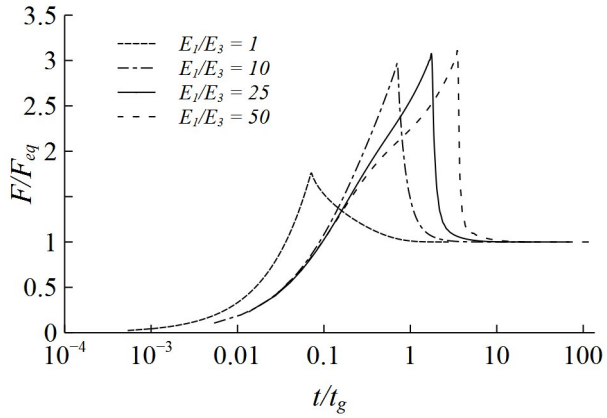

Figure 27: Effect of E_1/E_3 - Viscoelasticity in all directions. Model Parameters : E_3 = 1 MPa, $\nu_{21} = 0.49$, $\nu_{31} = 0.0$, $k = 5\text{x}10^{-15}$, ramp time = 131s, $c = 0.16$, $\tau_1 = 0.06$s, τ_2 = 201s, radius = 6.35mm, 10% strain

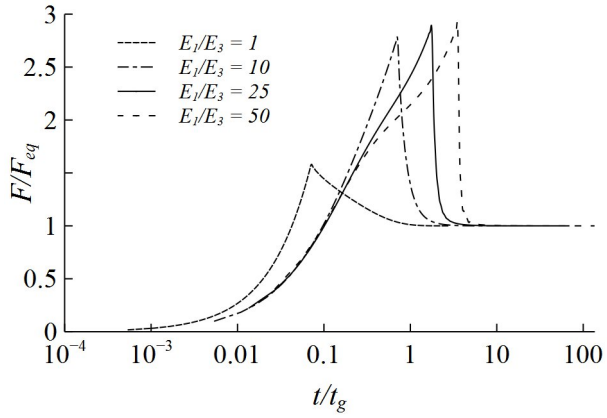

Figure 28: Effect of E_1/E_3 - Viscoelasticity in E_1 direction. Model Parameters : E_3 = 1 MPa, $\nu_{21} = 0.49$, $\nu_{31} = 0.0$, $k = 5\text{x}10^{-15}$, ramp time = 131s, $c = 0.16$, $\tau_1 = 0.06$s, τ_2 = 201s, radius = 6.35mm, 10% strain

was thought that a reduced radius would cause a higher fluid pressure in the axial and radial directions (the same pressure gradient exists in both directions) which would lead to a lower axial stress developed.

The next step in the analysis of this formulation was to curve fit it to some experimental data obtained in literature.

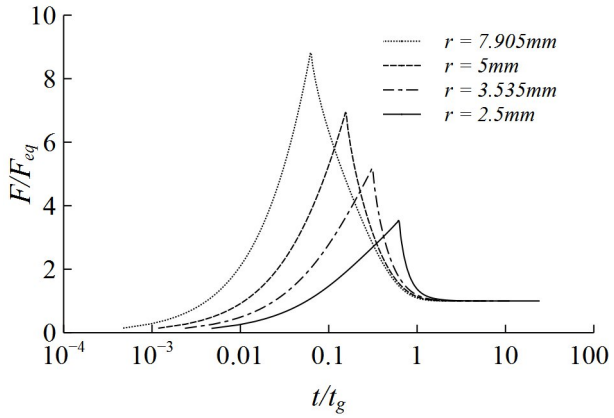

Figure 29: Effect of radius - Viscoelasticity in all directions. Model Parameters : E_1 = 4.55 MPa, E_3 = 0.47 MPa, ν_{21} = 0.49, ν_{31} = 0.0, k = 5x10^{-15}, ramp time = 131s, c = 0.16, τ_1 = 0.06s, τ_2 = 201s, 10% strain

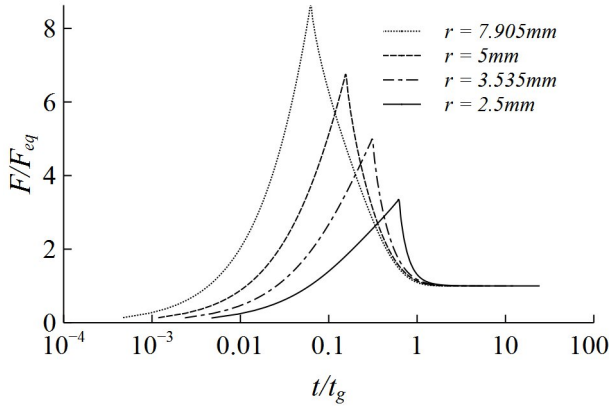

Figure 30: Effect of radius - Viscoelasticity in E_1 direction. Model Parameters : E_1 = 4.55 MPa, E_3 = 0.47 MPa, ν_{21} = 0.49, ν_{31} = 0.0, k = 5x10^{-15}, ramp time = 131s, c = 0.16, τ_1 = 0.06s, τ_2 = 201s, 10% strain

3.8. Curve Fitting

Experimental data for the slow strain rate (10^{-4} s^{-1}) unconfined compression of bovine articular cartilage from literature [81] was extracted using an image processing routine and was used to curve fit the biphasic, transversely isotropic and viscoelastic model. The diameter of the excised specimen were 4.78 mm and the max strain at the end of

ramping was 5 %. In their work, Huang et al [44] had devised a biphasic model with a conewise linear viscoelastic solid phase which could curve fit the experimental data accurately. Their curve fitting procedure [81], however, required the use of slow and fast confined, unconfined and dynamic compression experiments (to fix parameters or determine their ranges) in a multi-step and multi-objective optimization routine.

Figure 31 shows the curve fit and the parameters obtained under the assumption that viscoelasticity was present in both directions. An R^2 value of 0.991 was obtained for this fit. The slow compression data was also curve fit with the modified version of the aforementioned constitutive model such that only $E1$ was viscoelastic. An R^2 value of 0.992 was obtained for this fit. Figure 32 shows the result of this curve fit.

It is evident in figures 31 and 32 that the proposed constitutive model captures the tail of the stress relaxation experiment in a much more accurate manner as compared to the transversely isotropic and biphasic model of Cohen [6].

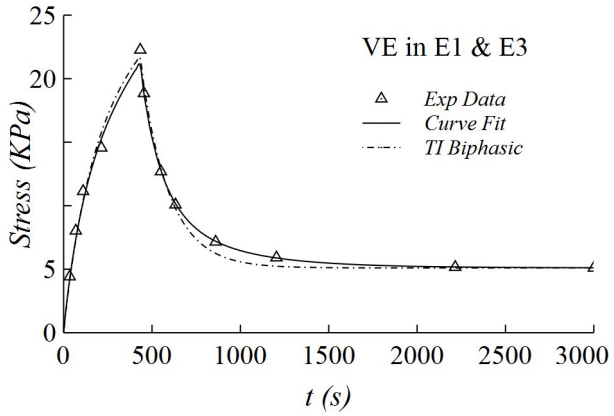

Figure 31: Curve fit for slow compression (Cartilage) under the assumption that viscoelasticity exists in all directions. Fit parameters: $E_1 = 0.64$ MPa, $E_3 = 0.408$ MPa, $k = 3.6\text{x}10^{-15}$ $c = 6.16$, $\tau_1 = 141.9$, $\tau_2 = 337.27$, 5% strain, $\text{R}^2 = 0.991$

It has been widely noted that the stress response at varying strain rates are governed by different mechanisms, therefore articular cartilage unconfined compression experimental data with fast ramp times were also used to curve fit the proposed constitutive models. The two versions of our proposed formulation were used to curve fit the fast data extracted from Huang et al [81] . The fast strain experimental data had specimen

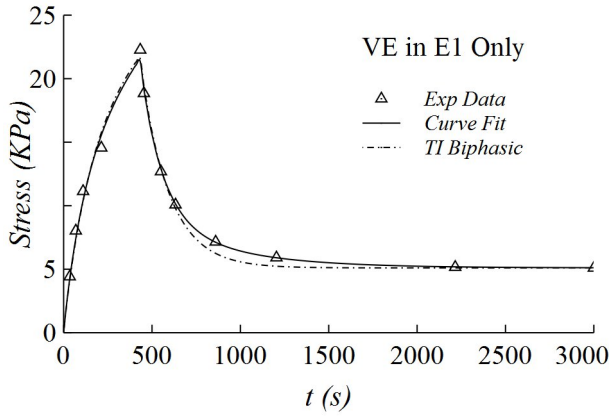

Figure 32: Curve fit for slow compression (Cartilage) under the assumption that viscoelasticity exists in E1 Direction. Fit parameters: $E_1 = 4.19$ MPa, $E_3 = 0.408$ MPa, $k = 1.1\text{x}10^{-15}$ $c = 0.69$, $\tau_1 = 52.62$, $\tau_2 = 112.204$, 5% strain, $R^2 = 0.992$

being compressed at much higher strain rates (1 s^{-1}). The cartilage specimen however had the same diameter. Plotting the curve fits in the normal time were inconclusive about the performance of the proposed model near the peak due to the fast ramp times as can be seen in figures 33 and 34 although the tail was captured much more accurately.

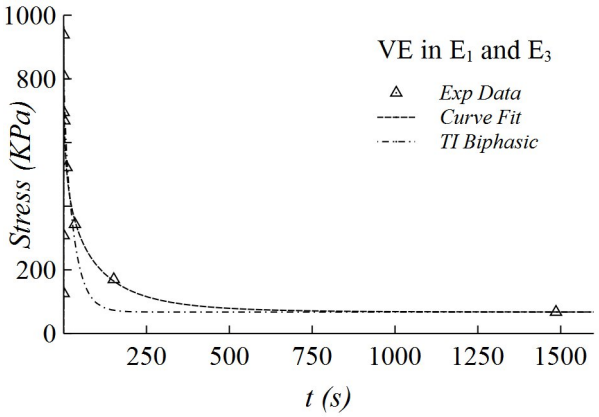

Figure 33: Curve fit for fast compression (in normal time) under the assumption that viscoelasticity exists in all directions - Inconclusive near peak. Fit parameters: $E_1 = 7.9$ MPa, $E_3 = 1.34$ MPa, $k = 0.78\text{x}10^{-15}$ $c = 0.13$, $\tau_1 = 0.054$, $\tau_2 = 329.28$, 5% strain, $R^2 = 0.991$

However, plotting the fits in logarithmic time as shown in figure 35 (in which viscoelasticity in all directions is assumed) showed a great improvement in the region of

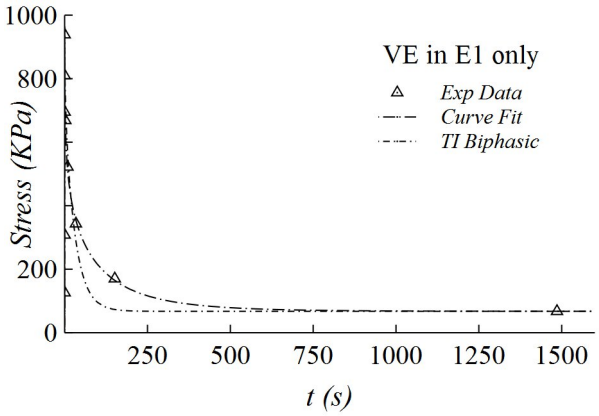

Figure 34: Curve fit for fast compression (in normal time) under the assumption that viscoelasticity exists in E1 direction - Inconclusive near peak. Fit parameters: $E_1 = 8.7$ MPa, $E_3 = 1.34$ MPa, $k = 0.74\text{x}10^{-15}$ $c = 0.14$, $\tau_1 = 0.052$, $\tau_2 = 236.03$, 5% strain, $R^2 = 0.991$

the peak. R^2 values of 0.991 were obtained for these fits. A great improvement over the transversely isotropic biphasic model of Cohen is also noticed as the peak stress and tail of the relaxation are both captured quite accurately.

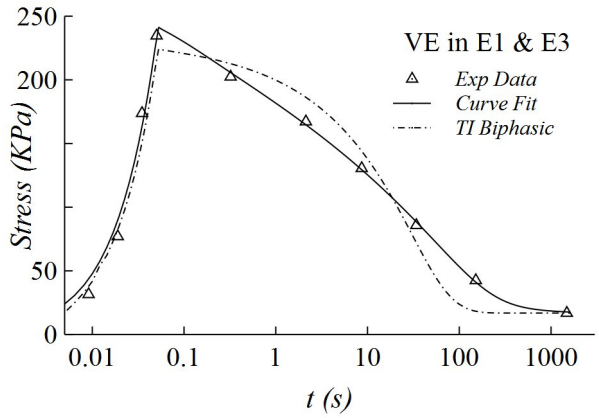

Figure 35: Curve fit for fast compression (Cartilage) under the assumption that viscoelasticity exists in all directions. Fit parameters: $E_1 = 7.9$ MPa, $E_3 = 1.34$ MPa, $k = 0.78\text{x}10^{-15}$ $c = 0.13$, $\tau_1 = 0.054$, $\tau_2 = 329.28$, 5% strain, $R^2 = 0.991$

The fast ramp data for unconfined compression was also used to curve fit the modified version of the TIVE constitutive model where viscoelasticity was assumed to exist only in the E1 direction. A fit of similar quality was obtained to the one which had

viscoelasticity in all directions as shown in figure 36. R^2 values of 0.991 were obtained for this optimization.

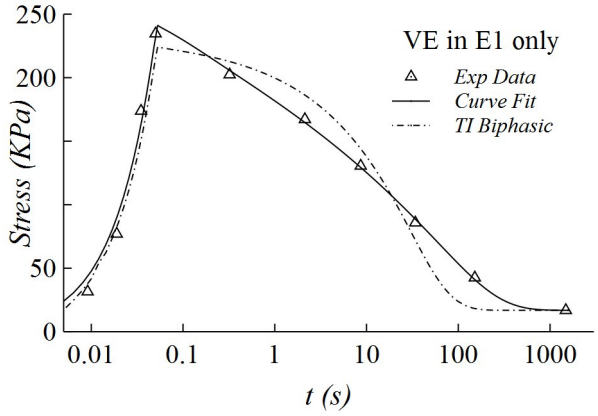

Figure 36: Curve fit for fast compression (Cartilage) under the assumption that viscoelasticity exists in E1 direction. Fit parameters: $E_1 = 8.7$ MPa, $E_3 = 1.34$ MPa, $k = 0.74\text{x}10^{-15}$ $c = 0.14$, $\tau_1 = 0.052$, $\tau_2 = 236.03$, 5% strain, $\text{R}^2 = 0.991$

CHAPTER 4

Conclusions and Future Work

4.1. Conclusions

A new constitutive model was developed for the mechanical behavior of articular cartilage in unconfined compression. This new model assumed a biphasic domain with a transversely isotropic and viscoelastic solid phase and an incompressible fluid phase. The formulation had a flexibility to account for viscoelasticity in either both radial and axial directions or radial direction alone under the assumption of a zero out-of-plane Poisson's ratio. A parametric study was carried out to observe the effect of the material parameters on the stress relaxation behavior of a hypothetical specimen. The base parameters of this study were chosen according to reported values in literature. When used in a preliminary curve fitting study, the model showed a marked improvement in predicting the stresses in the cartilage specimen compared to the biphasic, elastic and transversely isotropic model for the unconfined compression of cartilage particularly for high strain rates. For slow strain rates the tail of the relaxation curve was captured quite accurately although slightly higher residuals were obtained. This suggested an important role for solid phase viscoelasticity in the high strain rate experiments. On the other hand, it may be inferred that the fluid dependent viscoelasticity (caused by the biphasic mechanism) plays a more important role in the slow strain rate compression experiment.

The parametric study revealed that a higher strain rate caused a higher peak stress for both versions of the proposed formulation and that the increasing viscoelastic pa-

rameter c also caused an increase in the peak stress developed. The parameter τ_1 was seen to have a negligible effect on the stress relaxation behavior predicted by the model for ranges generally accepted in literature. τ_2 however, showed a significant effect on the peak stresses developed with increasing values causing a higher peak stress. The Poisson's ratio ν_{21} caused an increased peak stress as its value was increased from 0 to 0.49 whereas ν_{31} would cause a decrease in peak stress when increased by a physically feasible amount. If ν_{31} was increased to a limit where it would cause Δ_1 to be negative, our model would become physically invalid. Fluid permeability k had an inversely proportional effect on the peak stress developed by the model whereas the E_1/E_3 ratio had a directly proportional effect on the peak stress reached. All in all, it was seen that the ratio of the moduli, the ramp duration, fluid permeability and viscoelastic parameter c played the most important role in defining the peak stress. The parameter τ_2 was more influential on the curvature of the stress relaxation profile. Under the assumption that the out of plane Poisson's ratio ν_{31} was zero, the only parameter to effect the equilibrium stress was E_3 and the maximum strain reached. This behavior is concurrent with experimental observations.

As compared to the Huang model [44] for the unconfined compression behavior of articular cartilage, the proposed model may considered to be computationally inexpensive due to the lower number of parameters involved in optimization (just five for our model once Poisson's ratio and E_3 are fixed).

4.2. Future Work

4.2.1 Extension of Assumptions for Higher Complexity

The transversely isotropic, viscoelastic and biphasic model was modeled according to the assumptions of small deformation in unconfined compression. A next step would be to adapt the model to a confined compression experimental setup in which the boundary conditions for the model would change considerably (there would be no radial dis-

placement). The partial differential equation set up would depend on the independent variables z and t and the compressive movable head would be porous and free draining instead of rigid and impermeable. Similarly, the partial differential equations can also be set up for the shear and indentation experiment as well.

Experiments which may be carried out for large values of strain would not be suitable for prediction using this model due to the assumption of infinitesimal deformation. In that case, a finite deformation version of the model would be more appropriate. This continuum formulation would require the definition a strain energy function and subsequent tensor calculus to develop the transversely isotropic viscoelastic constitutive equation for the solid phase followed by integrating it with a fluid phase. Ning et al [82] have developed a transversely isotropic viscoelastic constitutive equation for brain-stem undergoing finite deformation in shear. Their relaxation mechanism is defined by a Prony series formulation. This may be the constitutive model for the solid phase which needs to be combined with the biphasic principle for an overall constitutive relationship for the unconfined compression experiment.

This model also assumes that the fluid pressure at any point in the specimen is purely a function of radial position and time. One could add a degree of complexity to this assumption by having different pressure fields in different directions since the fluid permeability in tissue may or may not be isotropic [83]. However, this would likely require the setup of partial differential equations depending on axial compression (i.e. in the z direction) as well which would lead to more than two coupled partial differential equations.

The transversely isotropic, viscoelastic and biphasic model can be modified to account for anisotropy in order to capture the mechanical behavior of certain types of soft tissue. Most tissue have been reported to have some degree of anisotropy under certain experimental conditions [84, 85, 86]. However, this case would also need the development of a newer type of geometry for the experiment which would necessitate a newer partial differential equation. Anisotropic materials also have more material constants so the model would be far more complex than it is now. There is also a chance that parameters may be excessively correlated needing sensitivity analyses and parameter

constraining from an optimization point of view.

4.2.2 Preliminary studies on Finite Difference Modeling

The proposed transversely isotropic, viscoelastic and biphasic model for cartilage may be validated using a finite difference method. To that end a preliminary study has been carried out to predict the stress response of the transversely isotropic and biphasic constitutive model. This study utilized a forward time marching scheme which plotted solutions for radial displacement and fluid pressure at discrete points through a two-dimensional grid (i.e. a grid in radius and time). These discrete solutions could then be used to determine the stress response of the simulated specimen.

For the purpose of validation, our preliminary solution for the finite difference approximation were compared to the analytical solution given in Cohen et al [6] where for the ramp we have -

$$f(t) = E_3\dot{\epsilon_0}t + E_1\frac{\dot{\epsilon_0}r_0^2}{C_{11}k}\Delta_3\left(\frac{1}{8} - \sum_{n=1}^{\infty}\frac{exp(-\alpha_n^2 C_{11}kt/r_0^2)}{\alpha_n^2[\Delta_2^2\alpha_n^2 - \Delta_1/(1+\nu_{21})]}\right) \tag{59}$$

and for the relaxation -

$$f(t) = E_3\dot{\epsilon_0}t_0 - E_1\frac{\dot{\epsilon_0}r_0^2}{C_{11}k}\Delta_3\left(\sum_{n=1}^{\infty}\frac{exp(-\alpha_n^2 C_{11}kt/r_0^2) - exp[-\alpha_n^2 C_{11}k(t-t_0)/r_0^2]}{\alpha_n^2[\Delta_2^2\alpha_n^2 - \Delta_1/(1+\nu_{21})]}\right) \tag{60}$$

As shown in figure 37, a good result was obtained for the finite difference approximation to the transversely isotropic and biphasic model. The challenge now lies in introducing viscoelasticity to the solid phase which would require the use of additional numerical integration through time (increasing computational cost significantly). For this purpose, the hereditary integral in time associated with linear viscoelasticity must be truncated after a sufficient distance is travelled into the past. The truncation should be devised in such a way that the accuracy of the approximation is not compromised.

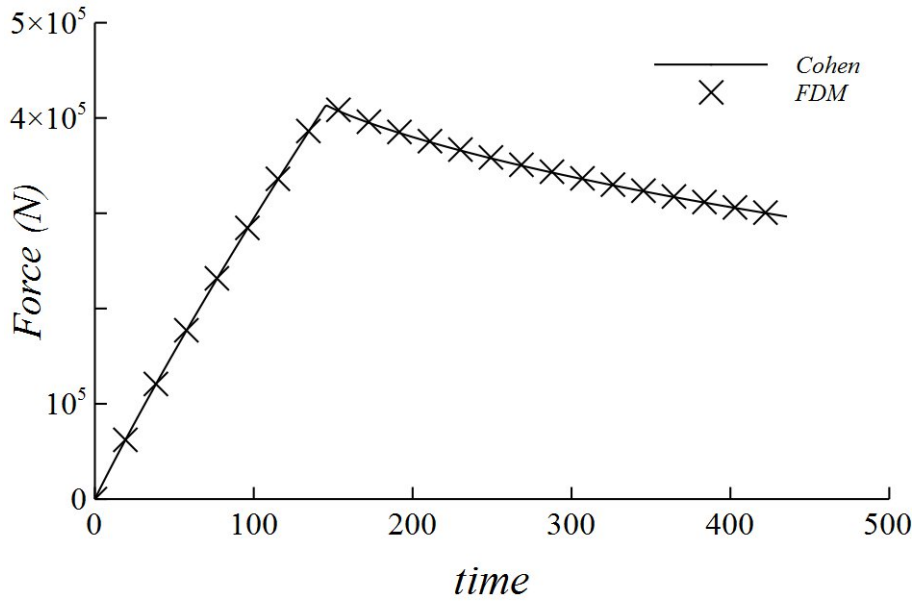

Figure 37: A Comparison of FDM and Analytical Solutions

4.2.3 Preliminary Studies on Quasilinear Viscoelastic Modeling for Unconfined Compression

According to general expression for QLV the stress relaxation behavior of soft-tissue can be given by -

$$\sigma(t) = G(t)\sigma(\epsilon)^{inst} + \int_0^t G(t-\tau)\frac{\partial \sigma^e(\epsilon)}{\partial \epsilon}\frac{\partial \epsilon}{\partial \tau}\partial\tau \tag{61}$$

The above expression of QLV has $\sigma(\epsilon)^{inst}$ as the instantaneous stress response and $\sigma^e(\epsilon)$ is the elastic stress-strain relationship for the material. For experimental data, no sudden jump is observed during the initial phase of the ramp and therefore the first term of the above expression can be dropped to give us the standard constitutive relationship for QLV used to characterize the mechanical behavior of various tissue for finite strain ramping -

$$\sigma(t) = \int_0^t G(t-\tau)\frac{\partial \sigma^e(\epsilon)}{\partial \epsilon}\frac{\partial \epsilon}{\partial \tau}\partial\tau \tag{62}$$

For the reduced relaxation function, Fung has proposed -

$$G(t) = \frac{1 + c[E_1(t/\tau_2) - E_1(t/\tau_1)]}{1 + c\log(\tau_2/\tau_1)} \tag{63}$$

where $E_1(x) = \int_x^\infty e^{-z}/z dz$ is the exponential integral of order 1, while c, τ_1 and τ_2 are material constants. For the instantaneous elastic response we propose to use -

$$\sigma^e(\epsilon) = A(\epsilon/\epsilon_0)^{1/2n} \tag{64}$$

Where, ϵ_0 is the strain at the end of finite ramping time, A and n are material parameters. It was decided to use the above expression because it would impart the desired degree of freedom to the mathematical formulation for capturing various stress response data. On substitution of equation (64) and (63) into (62) using the finite ramp approach [77] we can obtain -

$$\sigma(t) = \frac{A}{2\epsilon_0 n(1 + c\log[\tau_2/\tau_1])} \int_0^t \{1 + c(E_1[(t-\tau)/\tau_2] - E_1[(t-\tau)/\tau_1])\}(\tau/t_0)^{1/2n-1}\partial\tau \tag{65}$$

to estimate the stress response in the finite ramp duration. Similarly, the stress relaxation following the ramp can be predicted by -

$$\sigma(t : t \geq t_0) = \frac{A}{2\epsilon_0 n(1 + c\log[\tau_2/\tau_1])} \int_0^{t_0} \{1 + c(E_1[(t-\tau)/\tau_2] - E_1[(t-\tau)/\tau_1])\}(\tau/t_0)^{1/2n-1}\partial\tau \tag{66}$$

where t_0 is the duration of ramp. The strain history approach splits up the constitutive model into a piecewise function with two ranges in the dependent variable (time). The ranges are separated into the ramp and relaxation durations and it is assumed that the stress history beyond t_0 does not have a considerable effect on the mechanical response of the specimen. Equations (65) and (66) are curve fit simultaneously to experimental data to obtain the constants A, n, c, τ_1 and τ_2. A has the dimensions of stress, τ_1 and τ_2 are having the dimensions of time, n and c are dimensionless constants.

The equations (66) and (65) were used to curve fit the slow strain rate [6] and high strain rate compression data [81] from cartilage with improved performance as shown in figures (38) and (39).

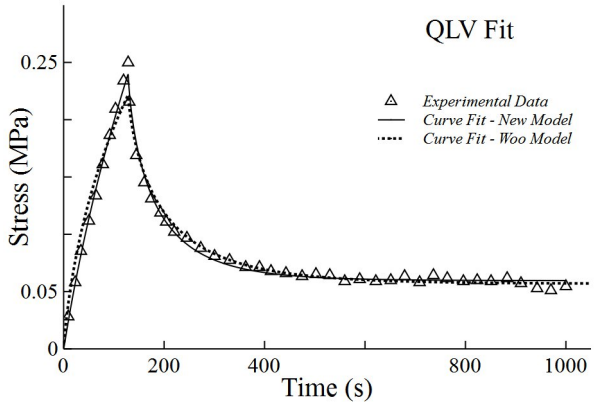

Figure 38: Curve fit for slow compression (Cartilage) using the new QLV model. Fit parameters: $A = 1602.28$ Pa, $n = 0.402$, $c = 2.83$, $\tau_2 = 152.18$s, $\tau_1 = 1\text{X}10^{-3}$, 10% strain, $R^2 = 0.994$

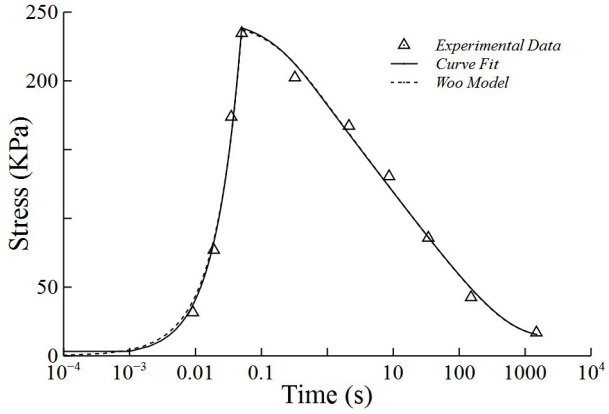

Figure 39: Curve fit for fast compression (Cartilage) using the new QLV model. Fit parameters: $A = 0.24$MPa, $n = 0.455$, $c = 1.97$, $\tau_2 = 820.89$s, $\tau_1 = 0.19$, 5% strain, $R^2 = 0.990$

The good performance of this model in both slow and fast compression experiments suggests a computationally efficient method to characterize the behavior of specimen for experimental purposes.

References

[1] Alice J Sophia Fox, Asheesh Bedi, and Scott A Rodeo. The basic science of articular cartilage: structure, composition, and function. *Sports Health: A Multidisciplinary Approach*, 1(6):461–468, 2009.

[2] Azadehsadat Hashemi Doulabi, Kibret Mequanint, and Hadi Mohammadi. Blends and nanocomposite biomaterials for articular cartilage tissue engineering. *Materials*, 7(7):5327–5355, 2014.

[3] Jaroslav Menčík, Li Hong He, and Michael V Swain. Determination of viscoelastic–plastic material parameters of biomaterials by instrumented indentation. *Journal of the mechanical behavior of biomedical materials*, 2(4):318–325, 2009.

[4] John Z Wu and Walter Herzog. Simulating the swelling and deformation behaviour in soft tissues using a convective thermal analogy. *Biomed. Eng. Online*, 1(8), 2002.

[5] Hamed Hatami-Marbini and Ebitimi Etebu. An experimental and theoretical analysis of unconfined compression of corneal stroma. *Journal of biomechanics*, 46(10):1752–1758, 2013.

[6] B Cohen, WM Lai, and VC Mow. A transversely isotropic biphasic model for unconfined compression of growth plate and chondroepiphysis. *Journal of biomechanical engineering*, 120(4):491–496, 1998.

[7] O Franke, K Durst, V Maier, M Göken, T Birkholz, H Schneider, F Hennig, and K Gelse. Mechanical properties of hyaline and repair cartilage studied by nanoindentation. *Acta Biomaterialia*, 3(6):873–881, 2007.

[8] Xiaodong Li, Yuehuei H An, Yii-Der Wu, Ying Ching Song, Yuh J Chao, and Chi-Hui Chien. Microindentation test for assessing the mechanical properties of cartilaginous tissues. *Journal of Biomedical Materials Research Part B: Applied Biomaterials*, 80(1):25–31, 2007.

[9] Reva C Lawrence, David T Felson, Charles G Helmick, Lesley M Arnold, Hyon Choi, Richard A Deyo, Sherine Gabriel, Rosemarie Hirsch, Marc C Hochberg, Gene G Hunder, et al. Estimates of the prevalence of arthritis and other rheumatic conditions in the united states: Part ii. *Arthritis & Rheumatism*, 58(1):26–35, 2008.

[10] Henry Gray. *Gray's Anatomy: With original illustrations by Henry Carter*. Arcturus Publishing, 2009.

[11] J Winslow Alford and Brian J Cole. Cartilage restoration, part 1 basic science, historical perspective, patient evaluation, and treatment options. *The American journal of sports medicine*, 33(2):295–306, 2005.

[12] Peter S Eggli, Wolfgang Herrmann, Ernst B Hunziker, and Robert K Schenk. Matrix compartments in the growth plate of the proximal tibia of rats. *The Anatomical Record*, 211(3):246–257, 1985.

[13] Farshid Guilak and Van C Mow. The mechanical environment of the chondrocyte: a biphasic finite element model of cell–matrix interactions in articular cartilage. *Journal of biomechanics*, 33(12):1663–1673, 2000.

[14] ER Myers, WM Lai, and VC Mow. A continuum theory and an experiment for the ion-induced swelling behavior of articular cartilage. *Journal of biomechanical engineering*, 106(2):151–158, 1984.

[15] A Maroudas, E Wachtel, G Grushko, EP Katz, and P Weinberg. The effect of osmotic and mechanical pressures on water partitioning in articular cartilage. *Biochimica et Biophysica Acta (BBA)-General Subjects*, 1073(2):285–294, 1991.

[16] Peter A Torzilli. Water content and equilibrium water partition in immature cartilage. *Journal of orthopaedic research*, 6(5):766–769, 1988.

[17] JA Buckwalter and HJ Mankin. Instructional course lectures, the american academy of orthopaedic surgeons-articular cartilage. part i: Tissue design and chondrocyte-matrix interactions*†. *The Journal of Bone & Joint Surgery*, 79(4):600–11, 1997.

[18] WC Hayes, LM Keer, G Herrmann, and LF Mockros. A mathematical analysis for indentation tests of articular cartilage. *Journal of biomechanics*, 5(5):541–551, 1972.

[19] AF Mak, WM Lai, and VC Mow. Biphasic indentation of articular cartilage—i. theoretical analysis. *Journal of biomechanics*, 20(7):703–714, 1987.

[20] GE Kempson, MAR Freeman, and SAV Swanson. The determination of a creep modulus for articular cartilage from indentation tests on the human femoral head. *Journal of biomechanics*, 4(4):239–250, 1971.

[21] RK Korhonen, MS Laasanen, J Töyräs, J Rieppo, J Hirvonen, HJ Helminen, and JS Jurvelin. Comparison of the equilibrium response of articular cartilage in unconfined compression, confined compression and indentation. *Journal of biomechanics*, 35(7):903–909, 2002.

[22] Roy Yoshikazu Hori and LF Mockros. Indentation tests of human articular cartilage. *Journal of Biomechanics*, 9(4):259–268, 1976.

[23] Wen Bin Li, JL Henshall, RM Hooper, and KE Easterling. The mechanisms of indentation creep. *Acta metallurgica et materialia*, 39(12):3099–3110, 1991.

[24] P-L Larsson and S Carlsson. On microindentation of viscoelastic polymers. *Polymer Testing*, 17(1):49–75, 1998.

[25] Matthieu Vandamme and Franz-Josef Ulm. Viscoelastic solutions for conical indentation. *International Journal of solids and structures*, 43(10):3142–3165, 2006.

[26] ML Oyen. Analytical techniques for indentation of viscoelastic materials. *Philosophical Magazine*, 86(33-35):5625–5641, 2006.

[27] JR Parsons and J Black. The viscoelastic shear behavior of normal rabbit articular cartilage. *Journal of Biomechanics*, 10(1):21–29, 1977.

[28] Hamed Hatami-Marbini. Viscoelastic shear properties of the corneal stroma. *Journal of biomechanics*, 47(3):723–728, 2014.

[29] LA Setton, Van C Mow, and DSrt Howell. Mechanical behavior of articular cartilage in shear is altered by transection of the anterior cruciate ligament. *Journal of Orthopaedic Research*, 13(4):473–482, 1995.

[30] AbdolRasol Rahimi. Characterization of Biomechanical Properties of the Bovine Cornea in Tension. Master's thesis, Oklahoma State University, Stillwater, USA, 2014.

[31] Hamed Hatami-Marbini. Hydration dependent viscoelastic tensile behavior of cornea. *Annals of biomedical engineering*, 42(8):1740–1748, 2014.

[32] Hamed Hatami-Marbini and Abdolrasol Rahimi. Effects of bathing solution on tensile properties of the cornea. *Experimental eye research*, 120:103–108, 2014.

[33] Robert M Schinagl, Donnell Gurskis, Albert C Chen, and Robert L Sah. Depth-dependent confined compression modulus of full-thickness bovine articular cartilage. *Journal of Orthopaedic Research*, 15(4):499, 1997.

[34] GA Ateshian, WH Warden, JJ Kim, RP Grelsamer, and VC Mow. Finite deformation biphasic material properties of bovine articular cartilage from confined compression experiments. *Journal of biomechanics*, 30(11):1157–1164, 1997.

[35] VC Mow, SC Kuei, WM Lai, and CG Armstrong. Biphasic creep and stress relaxation of articular cartilage in compression: theory and experiments. *Journal of biomechanical engineering*, 102(1):73–84, 1980.

[36] CG Armstrong, WM Lai, and VC Mow. An analysis of the unconfined compression of articular cartilage. *Journal of biomechanical engineering*, 106(2):165–173, 1984.

[37] WM Lai, Van C Mow, and V Roth. Effects of nonlinear strain-dependent permeability and rate of compression on the stress behavior of articular cartilage. *Journal of biomechanical engineering*, 103(2):61–66, 1981.

[38] AF Mak. The apparent viscoelastic behavior of articular cartilage—the contributions from the intrinsic matrix viscoelasticity and interstitial fluid flows. *Journal of biomechanical engineering*, 108(2):123–130, 1986.

[39] MH Holmes. Finite deformation of soft tissue: analysis of a mixture model in uniaxial compression. *Journal of biomechanical engineering*, 108(4):372–381, 1986.

[40] José Jaime García and Daniel Humberto Cortés. A nonlinear biphasic viscohyperelastic model for articular cartilage. *Journal of biomechanics*, 39(16):2991–2998, 2006.

[41] WM Lai, JS Hou, and VC Mow. A triphasic theory for the swelling and deformation behaviors of articular cartilage. *Journal of biomechanical engineering*, 113(3):245–258, 1991.

[42] Alain Curnier, Qi-Chang He, and Philippe Zysset. Conewise linear elastic materials. *Journal of Elasticity*, 37(1):1–38, 1994.

[43] Michael A Soltz and Gerard A Ateshian. A conewise linear elasticity mixture model for the analysis of tension-compression nonlinearity in articular cartilage. *TRANSACTIONS-AMERICAN SOCIETY OF MECHANICAL ENGINEERS JOURNAL OF BIOMECHANICAL ENGINEERING*, 122(6):576–586, 2000.

[44] Chun-Yuh Huang, Van C Mow, and Gerard A Ateshian. The role of flow-independent viscoelasticity in the biphasic tensile and compressive responses of articular cartilage. *Journal of biomechanical engineering*, 123(5):410–417, 2001.

[45] Mark R DiSilvestro, Qiliang Zhu, and Jun-Kyo Francis Suh. Biphasic poroviscoelastic simulation of the unconfined compression of articular cartilage: II — effect of variable strain rates. *Journal of biomechanical engineering*, 123(2):198–200, 2001.

[46] Mark R DiSilvestro, Qiliang Zhu, Marcy Wong, Jukka S Jurvelin, and Jun-Kyo Francis Suh. Biphasic poroviscoelastic simulation of the unconfined compression of articular cartilage: I—simultaneous prediction of reaction force and lateral displacement. *Journal of biomechanical engineering*, 123(2):191–197, 2001.

[47] Robert L Spilker, Jun-Kyo Suh, and Van C Mow. Effects of friction on the unconfined compressive response of articular cartilage: a finite element analysis. *Journal of biomechanical engineering*, 112(2):138–146, 1990.

[48] Robert L Spilker, Jun-Kyo Suh, and Van C Mow. A finite element analysis of the indentation stress-relaxation response of linear biphasic articular cartilage. *Journal of biomechanical engineering*, 114(2):191–201, 1992.

[49] Mark R DiSilvestro and Jun-Kyo Francis Suh. A cross-validation of the biphasic poroviscoelastic model of articular cartilage in unconfined compression, indentation, and confined compression. *Journal of biomechanics*, 34(4):519–525, 2001.

[50] J Soulhat, MD Buschmann, and A Shirazi-Adl. A fibril-network-reinforced biphasic model of cartilage in unconfined compression. *Journal of biomechanical engineering*, 121(3):340–347, 1999.

[51] LP Li, J Soulhat, MD Buschmann, and A Shirazi-Adl. Nonlinear analysis of cartilage in unconfined ramp compression using a fibril reinforced poroelastic model. *Clinical Biomechanics*, 14(9):673–682, 1999.

[52] W Wilson, CC Van Donkelaar, B Van Rietbergen, K Ito, and R Huiskes. Stresses in the local collagen network of articular cartilage: a poroviscoelastic fibril-reinforced finite element study. *Journal of biomechanics*, 37(3):357–366, 2004.

[53] LP Li, MD Buschmann, and A Shirazi-Adl. A fibril reinforced nonhomogeneous poroelastic model for articular cartilage: inhomogeneous response in unconfined compression. *Journal of biomechanics*, 33(12):1533–1541, 2000.

[54] Mansoor A Haider and Richard C Schugart. A numerical method for the continuous spectrum biphasic poroviscoelastic model of articular cartilage. *Journal of biomechanics*, 39(1):177–183, 2006.

[55] Paolo Provenzano, Roderic Lakes, Thomas Keenan, and Ray Vanderby Jr. Nonlinear ligament viscoelasticity. *Annals of biomedical engineering*, 29(10):908–914, 2001.

[56] Yuan-cheng Fung, Nicholas Perrone, and Max Anliker. Biomechanics, its foundations and objectives. 1972.

[57] John Wallis. *A treatise of algebra, both historical and practical*. London, 1685.

[58] Thomas Simpson. *Essays on Several Curious and Useful Subjects, in Speculative and Mix'd Mathematicks*. H. Woodfall, 1740.

[59] Adrien Marie Legendre. *Nouvelles méthodes pour la détermination des orbites des comètes*. Number 1. F. Didot, 1805.

[60] Carl Friedrich Gauss. *Theoria motus corporum coelestium in sectionibus conicis solem ambientium auctore Carolo Friderico Gauss*. sumtibus Frid. Perthes et IH Besser, 1809.

[61] Augustin Cauchy. Méthode générale pour la résolution des systemes d'équations simultanées. *Comp. Rend. Sci. Paris*, 25(1847):536–538, 1847.

[62] Kenneth Levenberg. A method for the solution of certain non–linear problems in least squares. 1944.

[63] Donald W Marquardt. An algorithm for least-squares estimation of nonlinear parameters. *Journal of the Society for Industrial & Applied Mathematics*, 11(2):431–441, 1963.

[64] William C Davidon. Variable metric method for minimization, aec res. *Dev. Rep. ANL*, 5990, 1959.

[65] Robert Hooke and T. A. Jeeves. "Direct search"solution of numerical and statistical problems. *Journal of the ACM (JACM)*, 8(2):212–229, 1961.

[66] WGRFR Spendley, George R Hext, and Francis R Himsworth. Sequential application of simplex designs in optimisation and evolutionary operation. *Technometrics*, 4(4):441–461, 1962.

[67] John A Nelder and Roger Mead. A simplex method for function minimization. *The computer journal*, 7(4):308–313, 1965.

[68] Russ C Eberhart and James Kennedy. A new optimizer using particle swarm theory. In *Proceedings of the sixth international symposium on micro machine and human science*, volume 1, pages 39–43. New York, NY, 1995.

[69] Alberto Colorni Marco Dorigo Vittorio Maniezzo. Distributed optimization by ant colonies. In *Toward a Practice of Autonomous Systems: Proceedings of the First European Conference on Artificial Life*, page 134. MIT Press, 1992.

[70] Rainer Storn and Kenneth Price. Differential evolution–a simple and efficient heuristic for global optimization over continuous spaces. *Journal of global optimization*, 11(4):341–359, 1997.

[71] Dervis Karaboga and Bahriye Basturk. A powerful and efficient algorithm for numerical function optimization: artificial bee colony (abc) algorithm. *Journal of global optimization*, 39(3):459–471, 2007.

[72] Xin-She Yang and Suash Deb. Cuckoo search via lévy flights. In *Nature & Biologically Inspired Computing, 2009. NaBIC 2009. World Congress on*, pages 210–214. IEEE, 2009.

[73] DT Pham, A Ghanbarzadeh, E Koc, S Otri, S Rahim, and M Zaidi. The bees algorithm–a novel tool for complex optimisation. In *Intelligent Production Machines and Systems-2nd I* PROMS Virtual International Conference 3-14 July 2006*, page 454. Elsevier, 2011.

[74] R Russell Rhinehart, Ming Su, and Upasana Manimegalai-Sridhar. Leapfrogging and synoptic leapfrogging: A new optimization approach. *Computers & Chemical Engineering*, 40:67–81, 2012.

[75] Zong Woo Geem, Joong Hoon Kim, and GV Loganathan. A new heuristic optimization algorithm: harmony search. *Simulation*, 76(2):60–68, 2001.

[76] Joseph E Olberding and JK Francis Suh. A dual optimization method for the material parameter identification of a biphasic poroviscoelastic hydrogel: potential application to hypercompliant soft tissues. *Journal of biomechanics*, 39(13):2468–2475, 2006.

[77] Steven D Abramowitch and Savio L-Y Woo. An improved method to analyze the stress relaxation of ligaments following a finite ramp time based on the quasi-linear viscoelastic theory. *Journal of biomechanical engineering*, 126(1):92–97, 2004.

[78] Roderic S Lakes. *Viscoelastic solids*, volume 9. CRC press, 1998.

[79] Frank R De Hoog, JH Knight, and AN Stokes. An improved method for numerical inversion of laplace transforms. *SIAM Journal on Scientific and Statistical Computing*, 3(3):357–366, 1982.

[80] Lori A Setton, Wenbo Zhu, and Van C Mow. The biphasic poroviscoelastic behavior of articular cartilage: role of the surface zone in governing the compressive behavior. *Journal of biomechanics*, 26(4):581–592, 1993.

[81] Chun-Yuh Huang, Michael A Soltz, Monika Kopacz, Van C Mow, and Gerard A Ateshian. Experimental verification of the roles of intrinsic matrix viscoelasticity and tension-compression nonlinearity in the biphasic response of cartilage. *Journal of biomechanical engineering*, 125(1):84–93, 2003.

[82] Xinguo Ning, Qiliang Zhu, Yoram Lanir, and Susan S Margulies. A transversely isotropic viscoelastic constitutive equation for brainstem undergoing finite deformation. *Journal of biomechanical engineering*, 128(6):925–933, 2006.

[83] WY Gu, XG Mao, RJ Foster, M Weidenbaum, VC Mow, and BA Rawlins. The anisotropic hydraulic permeability of human lumbar anulus fibrosus: influence of age, degeneration, direction, and water content. *Spine*, 24(23):2449, 1999.

[84] Chun-Yuh Huang, Anna Stankiewicz, Gerard A Ateshian, and Van C Mow. Anisotropy, inhomogeneity, and tension–compression nonlinearity of human glenohumeral cartilage in finite deformation. *Journal of biomechanics*, 38(4):799–809, 2005.

[85] JS Jurvelin, MD Buschmann, and EB Hunziker. Mechanical anisotropy of the human knee articular cartilage in compression. *Proceedings of the Institution of Mechanical Engineers, Part H: Journal of Engineering in Medicine*, 217(3):215–219, 2003.

[86] Nadeen O Chahine, Christopher CB Wang, Clark T Hung, and Gerard A Ateshian. Anisotropic strain-dependent material properties of bovine articular cartilage in the transitional range from tension to compression. *Journal of biomechanics*, 37(8):1251–1261, 2004.

[87] Wolfram Research, Inc. Mathematica 8.0.

Appendix A

De Hoog [79] Laplace Inversion Code - Wolfram Mathematica 10.1 [87]

```
a = 6;
ns = 20;
nd = 19;
alfa = {};
beta = {};
For[n = 1, n ≤ ns + 1 + nd, n++, alfa = Insert[alfa, a + (n - 1) * π * I, n];
  beta = Insert[beta, -Exp[a] * (-1)^n // N, n]];
n = Range[1, nd];
bdif = Reverse[Accumulate[Gamma[nd + 1] / Gamma[nd + 2 - n] / Gamma[n] / (2^nd) // N]];
For[n = 22, n ≤ ns + 1 + nd, n++, beta[[n]] = beta[[n]] * bdif[[n - 21]]];
beta[[1]] = beta[[1]] / 2;
s[t_] := alfa / t; (*Time is Not Dimensionalized*)
bt[t_] := beta / t;
I0[x_] := BesselI[0, x]
I1[x_] := BesselI[1, x]

constantA[E1_, E3_, nu21_, nu31_, kpar_, t_, c_, tau1_, tau2_] :=
 (C11[E1, E3, nu21, nu31] + C12[E1, E3, nu21, nu31] - 2 * C13[E1, E3, nu21, nu31]) /
  (C11[E1, E3, nu21, nu31] * Sqrt[f[E1, E3, nu21, nu31, kpar, t, c, tau1, tau2]] *
     I0[Sqrt[f[E1, E3, nu21, nu31, kpar, t, c, tau1, tau2]]] -
    I1[Sqrt[f[E1, E3, nu21, nu31, kpar, t, c, tau1, tau2]]] *
     (C11[E1, E3, nu21, nu31] - C12[E1, E3, nu21, nu31]))

Fnew[eps_, t_, E1_, E3_, nu21_, nu31_, kpar_, c_, tau1_, tau2_] :=
 (1 - Exp[-s[t] * t0[E1, E3, nu21, nu31, kpar]]) * eps /
       s[t]^2 * t0[E1, E3, nu21, nu31, kpar] *
  ((C11[E1, E3, nu21, nu31] * g[c, tau1, tau2, t]) * constantA[E1, E3, nu21, nu31, kpar,
      t, c, tau1, tau2] * (Sqrt[f[E1, E3, nu21, nu31, kpar, t, c, tau1, tau2]] *
        I0[Sqrt[f[E1, E3, nu21, nu31, kpar, t, c, tau1, tau2]]] / 2 -
       I1[Sqrt[f[E1, E3, nu21, nu31, kpar, t, c, tau1, tau2]]]) +
    C13[E1, E3, nu21, nu31] * g[c, tau1, tau2, t] *
     (constantA[E1, E3, nu21, nu31, kpar, t, c, tau1, tau2] *
        I1[Sqrt[f[E1, E3, nu21, nu31, kpar, t, c, tau1, tau2]]] - 1) +
    C33[E1, E3, nu21, nu31] * g[c, tau1, tau2, t])
btFnew[eps_, t_, E1_, E3_, nu21_, nu31_, kpar_, c_, tau1_, tau2_] :=
  bt[t] * Fnew[eps, t, E1, E3, nu21, nu31, kpar, c, tau1, tau2];
NewForce[eps_, t_, E1_, E3_, nu21_, nu31_, kpar_, c_, tau1_, tau2_] :=
  Total[Re[btFnew[eps, t, E1, E3, nu21, nu31, kpar, c, tau1, tau2]]] / 10^3 // N;
```

Figure 40: Laplace Inversion Code for the TI BPVE Model

Leapfrogging Optimizer - Wolfram Mathematica 10.1 [87]

User input

```
Clear["Global`*"](*Clearing all variables from memory*)

dv1min = 0.32 * 10^6;
dv1max = 0.68 * 10^6;
dv2min = 0.2 * 10^-15;
dv2max = 1.28 * 10^-15;
dv3min = 0;
dv3max = 1;
dv4min = 0.01;
dv4max = 0.77;
dv5min = 121;
dv5max = 775;(*This declares the range of particle
 values being initialized and the number of iterations*)

niter = 150 000 000;(*Number of iterations*)

npart = 100(*Number of Particles*);
```

Evaluation of particle costs

```
Plist = Flatten[{{Table[RandomReal[{dv1min, dv1max}], {i, 1, npart, 1}]},
    {Table[RandomReal[{dv2min, dv2max}], {i, 1, npart, 1}]},
    {Table[RandomReal[{dv3min, dv3max}], {i, 1, npart, 1}]},
    {Table[RandomReal[{dv4min, dv4max}], {i, 1, npart, 1}]},
    {Table[RandomReal[{dv5min, dv5max}], {i, 1, npart, 1}]}}, 1];
 (*Defining a first list of particles distributed in
 random space*)

Costslist = Table[Objfunc[Plist[[1, i]], Plist[[2, i]], eps,
    Plist[[3, i]], Plist[[4, i]], Plist[[5, i]]], {i, 1, npart, 1}];
 (*Calculating objective function cost for each set of decision variables*)

PrecValue = 0.000001;
```

Figure 41: Leapfrogging Optimizer Part 1

Leapfrogging Optimization - Rhinehart et al - 2012

```
Quiet[For[k = 1, k ≤ niter, k++,
  MinPos = Flatten[Position[Costslist, Min[Costslist]]][[1]];
  gbest = Flatten[{Plist[[1, MinPos]], Plist[[2, MinPos]],
     Plist[[3, MinPos]], Plist[[4, MinPos]], Plist[[5, MinPos]]}];
  MaxPos = Flatten[Position[Costslist, Max[Costslist]]][[1]];
  gworst = Flatten[{Plist[[1, MaxPos]], Plist[[2, MaxPos]],
     Plist[[3, MaxPos]], Plist[[4, MaxPos]], Plist[[5, MaxPos]]}];
  dv1new = gbest[[1]] - RandomReal[] * (gworst[[1]] - gbest[[1]]);
  dv2new = gbest[[2]] - RandomReal[] * (gworst[[2]] - gbest[[2]]);
  dv3new = gbest[[3]] - RandomReal[] * (gworst[[3]] - gbest[[3]]);
  dv4new = gbest[[4]] - RandomReal[] * (gworst[[4]] - gbest[[4]]);
  dv5new = gbest[[5]] - RandomReal[] * (gworst[[5]] - gbest[[5]]);
  Plist = ReplacePart[Plist, {{1, MaxPos} → dv1new, {2, MaxPos} → dv2new,
     {3, MaxPos} → dv3new, {4, MaxPos} → dv4new, {5, MaxPos} → dv5new}];
  Costslist = ReplacePart[Costslist,
    {MaxPos → Objfunc[dv1new, dv2new, eps, dv3new, dv4new, dv5new]}];
  Which[StandardDeviation[Plist[[1]]] / Mean[Plist[[1]]] < PrecValue &&
    StandardDeviation[Plist[[2]]] / Mean[Plist[[2]]] < PrecValue &&
    StandardDeviation[Plist[[3]]] / Mean[Plist[[3]]] < PrecValue &&
    StandardDeviation[Plist[[4]]] / Mean[Plist[[4]]] < PrecValue &&
    StandardDeviation[Plist[[5]]] / Mean[Plist[[5]]] < PrecValue,
   Break[], StandardDeviation[Costslist] < 0.000001, Break[]]]
```

Figure 42: Leapfrogging Optimizer Part 2

VITA

ROMIT MAULIK

Candidate for the Degree of

Master of Science

Thesis: A TRANSVERSELY ISOTROPIC VISCOELASTIC BIPHASIC MODEL OF ARTICULAR CARTILAGE IN UNCONFINED COMPRESSION

Major Field: Mechanical & Aerospace Engineering

Biographical:

Completed the requirements for the Master of Science in Mechanical & Aerospace Engineering at Oklahoma State University, Stillwater, Oklahoma in July,2015.

Completed the requirements for the Bachelor of Science in Mechanical Engineering at the Birla Institute of Technology, Mesra, India in July, 2012.

Experience:

Research Assistant August 2013 - Present

Computational Biomechanics Laboratory, OSU-Stillwater

- Developed a constitutive model for articular cartilage in unconfined compression.
- Carried out tensile and compressive experiments on connective tissue.

Teaching Assistant January 2014 - Present

MAE, OSU-Stillwater

- Helped undergraduate students in discussion sessions and office hours and helped instructor for grading of exams and homework